UNIVERSITY OF CALIFORNIA SAN DIEGO

Plasmonics in Quantum region

A dissertation submitted in partial satisfaction of the
requirements for the degree
Doctor of Philosophy

in

Electrical Engineering (Photonics)

by

Haoliang Qian

Committee in charge:

Professor Zhaowei Liu, Chair
Professor Yeshaiahu Fainman
Professor Eric E. Fullerton
Professor Yu-Hwa Lo
Professor Andrea Tao

2018

The dissertation of Haoliang Qian is approved, and it is acceptable in quality and form for publication on microfilm and electronically:

_____

_____

_____

_____

_____

Chair

University of California San Diego

2018

DEDICATION

To my family.

EPIGRAPH

Imagination is more important

than knowledge.

—Albert Einstein

TABLE OF CONTENTS

LIST OF FIGURES

LIST OF TABLES

ACKNOWLEDGEMENTS

Thanks to the advisor and all the committee members. Thanks to all the group members for every help.

Thanks to my family and especially to my wife, my forever princess.

Thanks to Department of Electrical and Computer Engineering, University of California San Diego.

Chapter 2, in part, is a reprint of the material as it appears in Nanophotonics 4, 413-418 (2015), Haoliang Qian, Yuzhe Xiao, Dominic Lepage, Li Chen, Zhaowei Liu. The dissertation author was the primary investigator and author of this paper.

Chapter 3, section 1, in part, has been submitted for publication of the material as it may appear in Light : Science & Applications (2018), Haoliang Qian, Shilong Li, Ching-Fu Chen, Su-Wen Hsu, Steven Edward Bopp, Qian Ma, Andrea R. Tao and Zhaowei Liu. The dissertation author was the primary investigator and author of this paper. Chapter 3, section 2, in part, is a reprint of the material as it appears in Nature Communication 7, 13153 (2016), Haoliang Qian, Yuzhe Xiao, Zhaowei Liu. The dissertation author was the primary investigator and author of this paper.

Chapter 4, section 1, in part, is a reprint of the material as it appears in Nature Photonics 12, 485-488 (2018), Haoliang Qian, Su-Wen Hsu, Kargal Gurunatha, Conor T Riley, Jie Zhao, Dylan Lu, Andrea R Tao, Zhaowei Liu. The dissertation author was the primary investigator and author of this paper. Chapter 4, section 2, in part, is currently being prepared for submission for publication of the material, Haoliang Qian, Shilong Li, Yingmin Li, Ching-Fu Chen, Yeon-Ui Lee, Steven Edward Bopp, Wei Xiong, and Zhaowei Liu. The dissertation author was the primary investigator and author of this paper.

VITA

2013	B. S. in Optical Engineering, Zhejiang University, China
2013-2018	Ph. D. in Electrical Engineering (Photonics), University of California San Diego

PUBLICATIONS

Qian, H., et al. Efficient light generation from enhanced inelastic electron tunnelling. *Nat. Photon.* 12, 485-488 (2018).

Lu, D., Qian, H., et al. Nanostructuring Multilayer Hyperbolic Metamaterials for Ultrafast and Bright Green InGaN Quantum Wells. *Adv. Mater.* 30, 1706411 (2018).

Xiao, Y., Qian, H., Liu, Z. Nonlinear Metasurface Based on Giant Optical Kerr Response of Gold Quantum Wells. *ACS Photonics* 5, 1654-1659 (2018).

Zhou, J., Qian, H., et al. Broadband Photonic Spin Hall Meta-Lens. *ACS Nano* 12, 82-88 (2017).

Wang, K., Qian, H., Liu, Z., Yu, P.K.L. Second-harmonic susceptibility enhancement in Gallium nitride nanopillars. *IEEE Electron Devices Technology and Manufacturing Conference (EDTM)* 28, 240-241 (2017).

Qian, H., Xiao, Y., Liu, Z. Giant Kerr response of ultrathin gold films from quantum size effect. *Nat. Commun.* 7, 13153 (2016).

Qian, H., et al. Quantum Electrostatic Model for Optical Properties of Nanoscale Gold Films. *Nanophotonics* 4, 413-418 (2015).

Qian, H., et al. Electrical Tuning of Surface Plasmon Polariton Propagation in GrapheneNanowire Hybrid Structure. *ACS Nano* 8, 2584-2589 (2014).

ABSTRACT OF THE DISSERTATION

Plasmonics in Quantum region

by

Haoliang Qian

Doctor of Philosophy in Electrical Engineering (Photonics)

University of California San Diego, 2018

Professor Zhaowei Liu, Chair

Plasmonics is a rapidly growing field of research that has been intensely investigated in the past few decades, for its abundant underlying physics and fruitful practical applications in nanophotonics, integrated optics, optical communication and information processing. Benefiting from the ability to confine light below the diffraction limit and its ultrashort response time ($\sim$ 100 fs), a plasmonic-based optical device provides an ideal platform for the study of ultra-strong light-matter interaction and has demonstrated great promise in the strong-coupling quantum system, ultra-fast optical modulators and efficient chip-scale nonlinearities. However, the traditional plasmonic materials and nano-structures suffer from several drawbacks that hinder the further development of plasmonics, such as high optical loss and a limited nonlinear response.

As a result, recent plasmonic-based devices have moved towards the quantum regime, searching for the better solution. And many recent reported results show noteworthy achievement. In this thesis, we have demonstrated that an efficient and tunable light source could be realized in delicately fabricated plasmonic nanostructures both in non-resonant and resonant conditions (with the metallic quantum well). It is done by engineering the electron wave-function coupling between plasmonic nanostructures (such as optical nano-antenna), and thus an efficient light generation is reached, which brings on-chip ultrafast and ultra-compact light sources one step closer to reality. In addition, we have shown that the nonlinear susceptibilities of ultra-thin plasmonic films could be engineered to be the state-of-the-art. It is done by introducing the quantum confinement into the plasmonic films (such as Au, Ag or TiN), so that a metallic quantum well is formed, which becomes new building blocks for the more complex plasmonic structures, such as metamaterials. This thesis starts from the theoretical investigation, followed by the nano-fabrication and experimental characterization, ends up with several interesting phenomena, their hidden physics and valuable applications. These quantum plasmonic materials and nano-structures realized in this thesis enable the further integration and functionalization of the plasmonic-based optical devices in the ultra-strong, efficient and fast light-matter interaction regime.

Chapter 1

Introduction

Plasmonics [1–4], a field which has emerged within the last decade has brought tremendous new opportunities to control light at scales previously thought impossible, e.g. the super-resolution imaging [5], optical nano-cavity [6], ultra-sensitive on-chip sensors [7] and high speed optical modulators [8, 9]. Owing to the giant field enhancement, large optical density of states (DOS) and related Purcell factor can be realized [10], which brings the engineering of the light emission efficiency and makes the high speed optical response achievable. One step further, strong coupling between the plasmonic resonance mode and the exciton states can be realized when the plasmonic mode volume reduced [11–13], as expected from the field confinement, which intrigues the fruitful underlying physics and gives the optical solutions for the quantum information processing.

Benefit from the ultra-high electric field enhancement and radiative coupling efficiency of designed plasmonic nanostructures [14], nonlinear optics, such as second/third harmonic generation (SHG/THG), have been demonstrated by low-intensity laser oscillators without costly power amplifiers in recent years [15, 16]. Nonlinear optics has been an extensive research focus since the generation of laser in the 1960s. The nonlinear interaction of light with matter itself leads to many interesting physical phenomena, such as harmonic generation [17], optical parametric

oscillation [18], and optical soliton [19, 20]. What′s more, the nonlinear effects also lead to many practical applications. For example, frequency-comb generated in optical cavities has been applied in metrology and optical communication system [21–25], and super-continuum generated through photonic crystal fibers [26, 27] are nowadays routinely used as a coherent broadband light source. However, despite much effort and many years of advancement in this field, chip-scale integrated nonlinear optics has yet to be realized due to the lack of materials with exceptionally high nonlinear responses.

1.1 Basic optical properties of surface plasmonics

Plasmonics, including the propagation surface plasmonics (SPP) and localized surface plasmonics (LSP), is an electromagnetic excitation existing at the interface between a dielectric and a metal. Surface plasmonics can be generated by either an irradiating electromagnetic wave or high-energy electrons [2]. Due to the ability to produce highly confined optical fields below the diffraction limit, surface plasmonics has wide scientific and technological applications such as plasmonic lasers, optical antennas, optical sensors, and subwavelength waveguides.

Typical plasmonic materials are noble metals such as silver, gold and aluminum, as well as some of the transition metal nitrides, such as TiN and ZrN [28]. Under the classical pictures, the plasmonic materials can be treated as free electrons with high electron density and thus, the optical properties can be modeled as the Drude model [29], shown in the Eq. (1.1).

$$\varepsilon = 1 - \frac{w_p^2}{w^2 + iw\gamma} \tag{1.1}$$

where the w_p is the bulk plasmon frequency and γ is the damping rate. The most simple geometry sustaining surface plasmon polariton is that of a single, flat interface between the metal (silver as an example here) and dielectric SiO_2 as schematically drawn in Figure 1.1.

To quantify the SPP properties, the wave equation is needed, which can be derived from

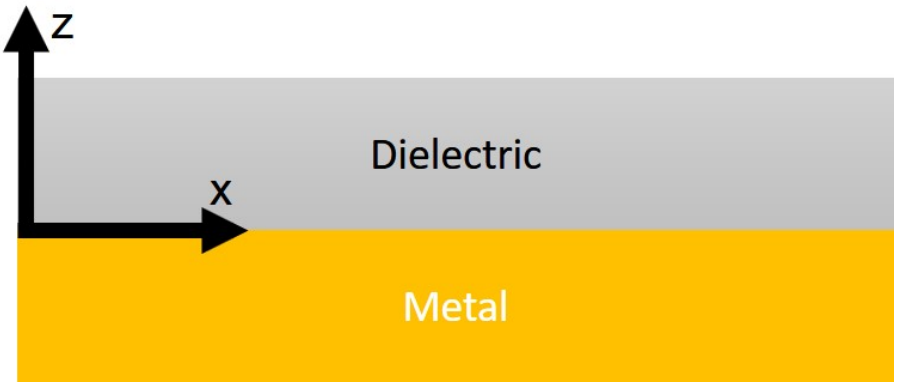

Figure 1.1: Geometry for SPP at a single interface between a metal and a dielectric.

the Maxwell's equation. We skip all the derivation here and the wave equation for the surface plasmonics is deduced as the following equation 1.2.

$$\frac{\partial^2 E(z)}{\partial z^2} + (k_0^2 \varepsilon) E = 0 \tag{1.2}$$

By solving the wave equation, we would get all the solutions for the plasmonic modes and it is found out that only TM mode exists for the SPP [2]. One of the most important results from the wave equation is the dispersion relation of the SPP. For the single interface between the silver and the SiO_2 as an example, the dispersion relation is shown in the Fig. 1.2.

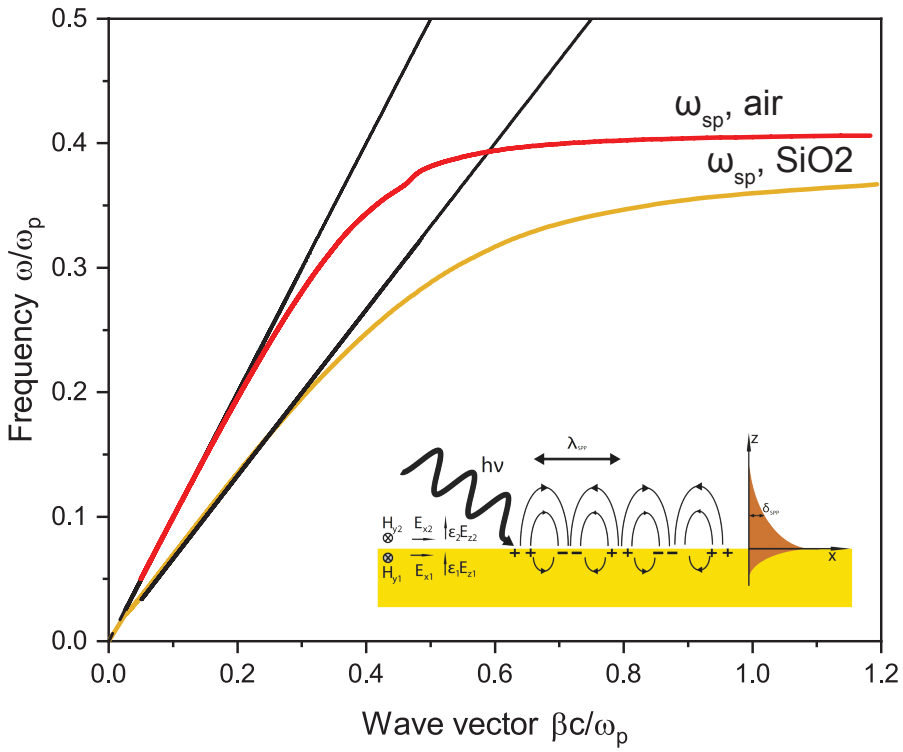

Figure 1.2: Dispersion relation of the SPP in the sinlge Ag/SiO_2 and Ag/air interface. The SPP wave is schematically illustrated in the inset.

Another type of surface plasmonics is the localized surface plasmons. Localized surface plasmons, compared with the SPP, are non-propagating excitations of the conduction electrons in metallic nanostructures coupled to the electromagnetic field. These modes arise naturally from the scattering/absorption of a sub-wavelength metallic nanoparticles/nanostructure in an oscillating electromagnetic field, where the curved surface of the particle exerts an effective restoring force on the driven electrons, so that a resonance can arise, leading to the field amplification both inside and in the near-field area outside the particle. Due to the curved surface, the localized plasmon resonances can be excited by direct light illumination, with the momentum mismatch fulfilled by the light scattering on the surface, in contrast to propagating SPP, where the momentum conservation need to be considered for the wavelength dispersion. A typical localized plasmon excitation of the Au particles are presented with the scattering response in Fig. 1.3.

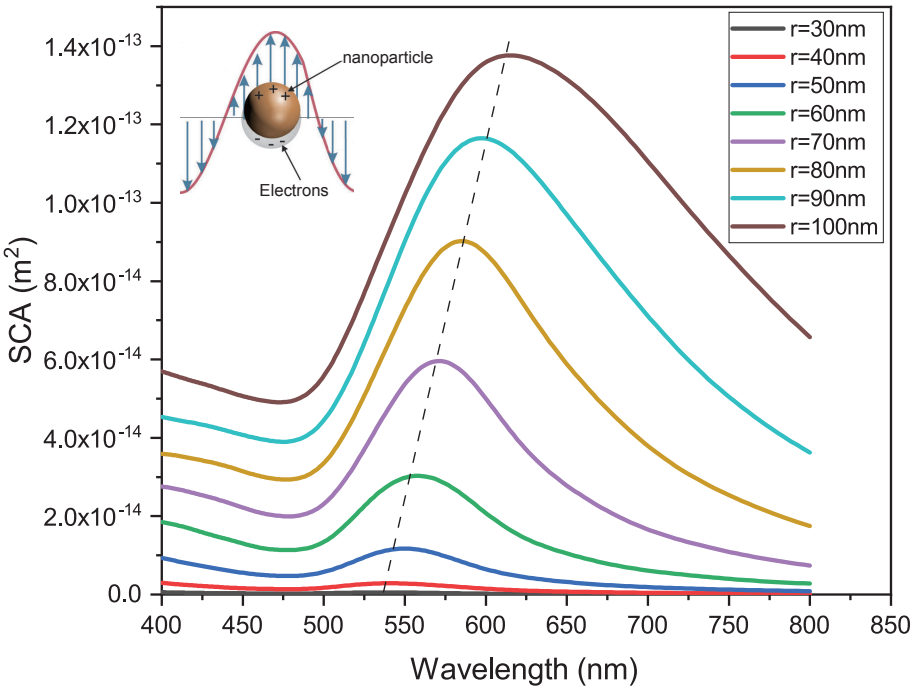

Figure 1.3: Au particle size-dependent (radius r) scattering resonance, where the peak wavelength corresponds to the localized surface plasmon.

In Fig. 1.3, the scattering cross section (SCA) is simulated and plotted for different radii of the Au particle, where the resonance peak wavelength is gradually increased with the radius, as marked by the dashed line. The inset shows how the incident electromagnetic wave drive the electron cloud in the metallic nanoparticles.

1.2 Quantum size effect on optical material properties

With the development of nano-fabrication techniques, the dimension of plasmonic devices has been shrunk into the nanoscale [30], where the impact of quantum physics becomes important [31, 32]. Various nanometer scale plasmonic devices have shown new features that differ from traditional plasmonics [31–34]. Over the past few years, the impact of quantum effects on the linear properties of plasmonic devices has been examined from both experimental [32, 35] and theoretical [36–38] point of views. One of the most important effects from the quantum

plasmonic devices is the quantum confinement of the free electrons in the plasmonic materials, which can be achieved by reducing the dimension of the devices. This will results into two major consequences: 1. the electron wave-functions will be extended to the width of the quantum well, and thus the increasing of the electron dipole moment. 2. There exists the optical transition between each electronic eigen-state, which will affect both the linear and nonlinear optical properties. A typical metallic quantum well (TiN/Al_2O_3) is plotted in Figure 1.4. The electronic eigen-states and eigen-function are clearly visible, together with the electronic dispersion for these subbands, where the optical transition can happen near the Fermi level. The electron wave-function engineering of the plasmonic materials opens a new realm for the design of the linear/nonlinear optical properties in the visible/near infrared region where the typical plasmonic material lies in.

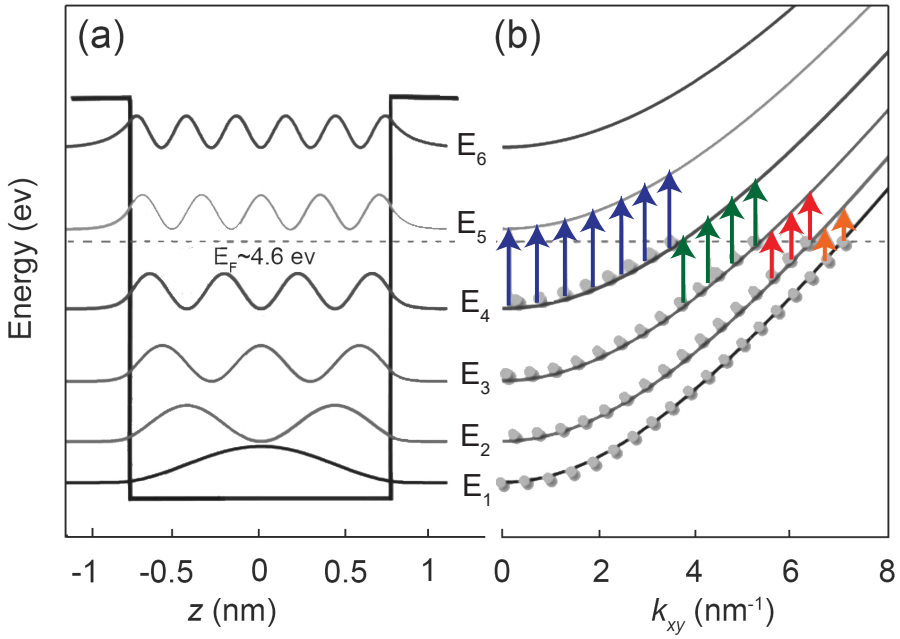

Figure 1.4: Band structure of an 1.5 nm TiN/Al_2O_3 quantum well. (a) Energy levels of the metallic quantum well. (b) Electronic dispersion of the subbands. The dashed line indicates the Fermi energy. The arrows indicate the main optical transitions that can take place in the structure.

1.3 Applications of surface plasmonics in quantum region

With the existence of the quantized energy states, the engineering of the large nonlinear coefficient on the plasmonic materials will come up at once for the efficient light-matter interaction applications. With the large free electron density (on the order of $10^{28}m^{-3}$) and giant dipole transition moment (on the order of the quantum well width), the nonlinear susceptibility will be order-of-magnitude higher than the classical nonlinear medium, such as gold, and traditional nonlinear crystals, such as SiO_2 and $LiNbO_3$. Due to the promising nonlinear properties from the metallic quantum well, a lot of vital nonlinear applications, such as pulse limiter, wave-mixer, super-continuum generation or frequency comb can be realized on the nanoscale level.

As we mentioned in the early part of this chapter, besides the low nonlinear response, the plasmonic materials also suffers from the loss. In this case, an promising and interesting direction will be the plasmonic enhancement light emission in the quantum region. As we know that, the traditional plasmonic material possess the Purcel effect, which can enhance the light emission process, such as intensity and speed [10, 39]. With the plasmonic materials entering into the quantum region, light emssion process can be directly engineered through the electronic energy states and corresponding wave-functions. For example, the traditional semiconductor quantum dot excitons can be coupled with the intersubband transitions (intersubband plasmon) in metallic quantum well where the light emission process will be modified to be faster and brighter. What's more, the metallic quantum well can be inserted into traditional plasmonic nano-junctions that is based on the inelastic tunneling process, to form the resonant tunneling junction, so that the light generation efficiency can be greatly promoted into more than 20% level.

Future application may focus on the combination of the electron wave-function engineering in quantum sized materials with the specific design of the photonic or plasmonic cavities (or waveguide), as well as the coupling between each plasmon system, which would enable the efficient light-matter interaction even with the single-photon manipulation.

Chapter 2

Theoretical modeling

Plasmonics that utilizes the interaction of light and charged particles, such as electrons in metals, has been an area of interest for decades. It has led to many fascinating applications in a unforeseen degree of freedom. With the development of nano-fabrication techniques, the dimensions of the plasmonic device have been shrunk into the nanoscale. Under this context, the field of quantum plasmonics, which combines quantum mechanics with plasmonics, has emerged and drawn much attention recently. In order to explore the underlying physics for the plasmonics in quantum region, a theoretical model which can accurately calculate or predict the plasmonic materials' permittivities, including the linear permittivity and nonlinear susceptibility, is extremely in demand. There has been several approaches to deal with quantum plasmonics, for example, nano particles with quantum size model [35, 38], quantum correlated model [37] or density function theory [40]. The agreement between those theoretical models and experimental result, however, is only qualitative, and a more accurate model is still not available. Here, we choose the ultra-thin metallic film as a platform to study the quantum plasmonics and propose a quantum electrostatic model to deal with the linear and high order optical properties in the metallic quantum well system.

2.1 Approach for the quantum size effect

Although the quantum behavior has been extensively explored with various theoretical models in the context of semiconductor quantum wells [41], these models cannot be directly applied to metals, due to the large electron density and different band structures. Ultra-thin plasmonic films had previously drawn wide research interests in the context of quantum physics [42–45], and recent effort has been focused on the optical properties of ultra-thin metal films with thickness of a few nano meters. Besides the classical Drude model [46], several new theoretical methods have been proposed, such as quantum size model [35,38], quantum correlated model [37] or density function theory [40]. The agreement between those theoretical models and experimental result, however, is only qualitative, and a more accurate model is still not available according to our knowledge. Therefore, we propose a Quantum Electrostatic Model (QEM) to study the electron dynamics within a metallic quantum well. The major concern for this QEM model is the consideration of the electron-electron interaction and re-distribution within the quantum wells due to the large electron density. More specifically, a theory based on the self-consistent solution of Schrdinger equation and Poisson equation is applied for the calculation of the ultra-thin plasmonic films.

We first choose the ultrathin gold film for studying the QEM model. The gold film is grown on top of a quartz substrate with the thickness about 2.5 nm. The quantum confinement effects would become pronounced when the thickness of the film is comparable to the de Broglie wavelength of the electron. For such ultra-small thickness, a quantum well would be formed by the potential barrier from vacuum and quartz on two sides of the gold, and the continuum energy levels of the free electrons in the case of bulk gold will become discrete in the metallic quantum well.

Magnetron sputtering is being used for the film growth, and the growth conditions, including the pressure, gas flow, power, et.al, have been optimized to give better uniformity and

less surface roughness. Figure 2.1 shows the atomic force microscopy (AFM) image of one of our optimized 2.5 nm gold film samples. As can be seen here, although the film is not perfect flat as indicated by the surface fluctuations, it is not broken at 2.5 nm thickness level. Also shown in the lower inset is the statistics of the film thickness variations, where we can see the surface roughness (root mean square) of the film thickness is about 0.5 nm.

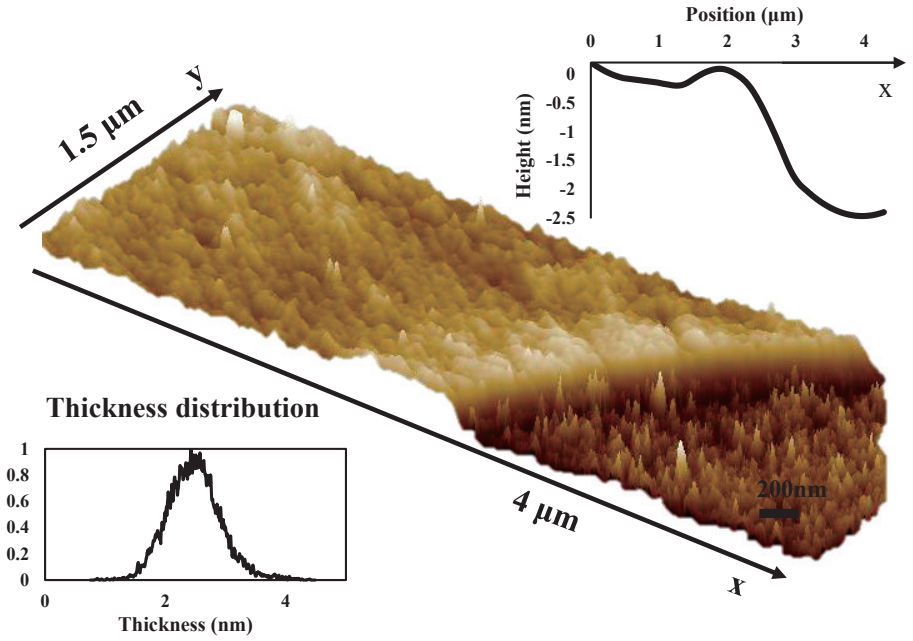

Figure 2.1: AFM image of the 2.5 nm gold thin films. Here shows the film edge on the substrate. The upper inset shows the averaged height on the both side across the edge (the mean thickness), indicating the mean thickness of the film is about 2.5 nm. The lower inset shows the surface roughness is around 0.5 nm.

2.2 Linear material properties with quantum size effect

In order to obtain the linear material properties of the ultra-thin metallic film, we developed an extraction strategy, which combines the multilayer transfer matrix method [47] and a two dimensional Newton iteration method. More specifically, the linear material properties are extracted from the reflection and transmission measurement under fixed angle and polarization with the transfer matrix method. Since the transfer matrix method is universal for all the film

thickness and as long as the reflection and transmission measurement is accurate, the extracted material properties will be valid. The measured spectral reflection and transmission are shown in Fig. 2.2(a) and (b), and the corresponding extracted n and k for films with different thicknesses are plotted in Fig. 2.2(c) and (d), respectively. Also the n, k value for bulk gold from Johnson and Christy are plotted using dashed-black curves. Both n and k for 7 nm and 15 nm are quite similar and converge to bulk values, which are expected. The case of 2.5 nm film is quite different: the increase of n and the decrease of k make the 2.5 nm gold film less like metal. Moreover, unlike the n and k for thicker films (where both of which increase with wavelength), n decreases, while k increases with wavelength for 2.5 nm film in the 1 to 2 μm wavelength range.

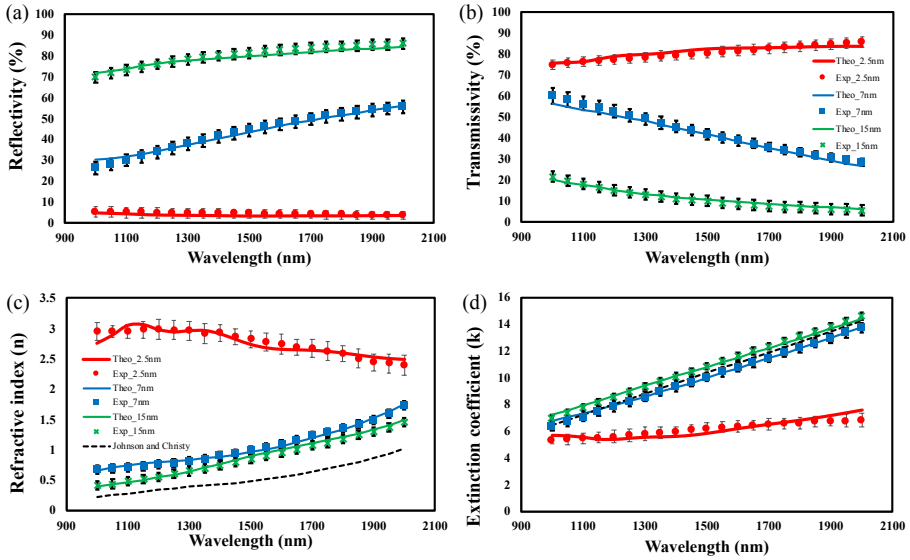

Figure 2.2: Reflection (a) and transmission (b) with refractive index n (c) and extinction coefficient k (d) for the 2.5 nm, 7 nm, and 15 nm samples. Optical constants of the thin film samples are extracted from reflection/transmission data. n and k for 7 nm and 15 nm are very similar, and converge to bulk values (dash line, tabulated data from Johnson and Christy). The behavior for the 2.5 nm sample is significantly different from those for 7 and 30 nm sample, indicating the impact of quantum size effect. Predictions from our QEM are also plotted, all showing good agreement with experimental result.

Clearly, such a distinct behavior of the optical constants is related to the change in film thickness. Based on the observed experimental results. In the following paragraphs, we will describe the Quantum Electrostatic Model in details and try to calculate the optical properties by

considering the electron dynamics within the thin metallic films in the QEM. The starting point is the Schrdinger equation:

$$\frac{1}{2m}[\widehat{\vec{p}}+\frac{e}{c}\vec{A}]^2\,|\varphi\rangle+V(\vec{r})\,|\varphi\rangle+\phi(\vec{r})\,|\varphi\rangle=E\,|\varphi\rangle \tag{2.1}$$

In the Eq. 2.1, the m and e are the effective mass and charge of the free electrons, $\widehat{\vec{p}}$ is the momentum operator, c is the speed of light in vacuum, $\vec{A}$ and $\phi(\vec{r})$ are the vector and scalar potential associated with the applied electromagnetic field, which can be set as zero in our case, and $V(\vec{r})$ is the potential determined by the metallic quantum well structure. The solution from Schrdinger equation alone, however, is not self-consistent because the potential $V(\vec{r})$ is modified by the electron distribution inside the quantum well. To account for this effect, Poisson equation needs to be included. The Schrdinger equation is firstly solved with an initial guess for the potential $V(\vec{r})$ from the shape of the quantum well. Electron density is then obtained from the eigen-energies E_k and wave functions φ_k following

$$\rho(z)=\sum_{k=1}|\varphi_k(z)|^2\frac{m}{\pi\hbar^2}\int_{E_k}^{\infty}\frac{dE}{1+e^{(E-\mu)/k_BT}} \tag{2.2}$$

where μ is the Fermi energy, $\hbar$ is the reduced Planck constant, k_B is the Boltzmann constant, T is kelvin temperature and assuming the metallic quantum well is in the z direction. Poisson equation is then solved to find the new potential based on the electron density calculated from Eq. 2.3

$$\nabla[\varepsilon_0\varepsilon_{static}\nabla V(z)]=-\rho(z) \tag{2.3}$$

where ε_0 is the vacuum permittivity and ε_{static} is the relative static permittivity of the ultra-thin gold film. The updated potential $V(z)$ is then substituted back into the Schrdinger equation to solve for the new eigen energies and wave functions. This iteration process is repeated until finally a self-consistent electron density $\rho(z)$ and potential $V(z)$ are obtained.

Once the eigen energy E_n and eigen wave function $|\varphi_n\rangle$ are solved from the iteration process, the permittivity of the metallic quantum well can be calculated using the following expression:

$$\varepsilon = 1 - \frac{\omega_p^2}{\omega^2} = \frac{8\pi e^2}{\Omega m^2 \omega^2} \sum_{ij} \frac{f_i E_{ij} |\langle i| \widehat{\vec{p}} |j\rangle|^2}{E_{ij}^2 - \hbar^2 \omega^2} \tag{2.4}$$

where the plasma frequency ω_p is determined by the electron density ρ_e through $\omega_p^2 = \rho_e e^2 / m\varepsilon_0$, Ω is the volume of the quantum well, $E_{ij} = E_i - E_j$ is the difference in eigen energies. $f_i = 1/(1 + e^{(E_i - \mu)/k_B T})$ is the Fermi-Dirac occupation factor for the i_{th} state.

The above iteration assumes a quantum well from a perfect metallic film, where the relaxation process of electrons is neglected. In reality, electrons are affected by the relaxation process due to either lattice vibration (thermal excitations), or static imperfections (such as impurities) or the impact of boundaries. So it is necessary to include this effect as well. An electron relaxation time τ is used to quantify the strength of this effect. Such effect cannot be included simply by replacing ω with $\omega + i/\tau$ in Eq. 2.4 because it fails to conserve the local electron number. In order to account for the relaxation process, we adopted the model from Mermin [48] and the permittivity is obtained in the following form

$$\varepsilon_{corr}(\omega) = 1 + \frac{(1 + i/\omega\tau)(\varepsilon - 1)}{1 + (i/\omega\tau)(\varepsilon - 1)/(\varepsilon_{static} - 1)} \tag{2.5}$$

The refractive index n and extinction coefficient k are finally obtained as: $n = \mathrm{Re}(\sqrt{\varepsilon_{corr}})$ and $k = \mathrm{Im}(\sqrt{\varepsilon_{corr}})$.

Numerical simulations based on the QEM are preformed for the metallic thin films with different thicknesses. Calculated n and k, and the corresponding RT curves are plotted in Fig. 2.2, where theoretical predictions match quite well with experimental results for all 3 different thickness samples from bulk metal to metallic quantum wells. This clearly shows that QEM is valid in describing the electron dynamics inside a metallic quantum well. The reason for such a different behavior for the 2.5 nm thin film as compared to the thicker ones (7nm and 15nm) is the

modification of the quantum corrected terms (the last term on the right hand side of Eq. 2.4) to the material properties. In the limit of bulk gold film, the energy states of the free electrons are continuum and the wave functions are plane waves, which will lead the quantum-corrected term to go to zero. The contribution from this term is no longer zero in the quantum region, where the free electrons are quantized. The eigen-states and eigen-function for the 2.5 nm and 15 nm metallic quantum well is provided in Fig. 2.3.

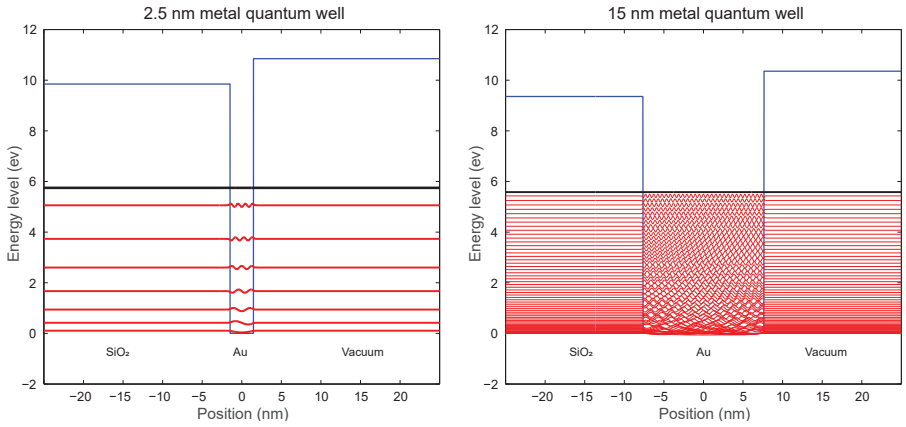

Figure 2.3: Eigen energies and wave functions for the 2.5 nm (left) and 15 nm (right) quantum well. The values of the eigen-energies are indicated by the height of each horizontal line (red), while the black line indicates the Fermi level.

It is important to note that our model characterizes the behavior of free electrons under the impact of quantum size effect. It can be applied to materials as long as their optical properties can be approximated by free electron model, and can be very easily generalized to other metallic quantum structures, such as quantum wires and quantum dots. Other effects that are related to the band structure of gold atom itself, such as the interband transition, exciton absorption are not covered in this model, but can be included by adding the additional terms. For example, the interband transition can be included through $\varepsilon = \varepsilon_{corr} + \varepsilon_{IB}$, where the ε_{IB} represents the interband transition [49].

The parameters used for the numerical simulations with the 15 nm, 7 nm, and 2.5 nm thick films are summarized in Table 2.1. As expected, the parameters of 15 nm samples are

almost identical to those of bulk material. As film thickness is reduced, the electron effective mass m, relaxation time τ, and the absolute value of static permittivity ε_{static} all decrease. The reduction of the relaxation time agrees with previous investigation [50,51], and can be understood from the fact that the impact of boundaries and imperfection from thickness variation become more and more important as film thickness is reduced. The effective mass of thin gold film was experimentally measured to be smaller than its bulk value previously. The static permittivity has been investigated for thin films and was also found to decrease as thickness is reduced. All parameters are in reasonable range and agree with the previous findings.

Table 2.1: Simulation parameters for the 2.5 nm 7 nm,,and 15 nm thick thin films

Thickness (nm)	m	τ(fs)	ε_{static}
2.5	$0.36m_e$	4.54	-1300
7	$0.81m_e$	7.05	-7000
15	m_e	10	-15000

As a final comparison, we plot the calculated RT curves from Drude model, nonlocal model, quantum size model and QEM with 2.5 nm and 7 nm gold film, together with the measured experimental curves in Fig. 2.4. For the Drude model, we use a plasma frequency $\omega_p = 1.38 \times 10^{16}\ rad/s$ and relaxation time $\tau = 9.3$ fs, which are the typical values for gold. For the nonlocal model, we adopt the model from Ref. [36], and use the parameters for gold provided within it. For the quantum size model, we use the model from Ref. [38], and use the same parameters listed in Table 2.1.

As can be seen from Fig. 2.4, Drude model can give reasonable good predictions of RT curves for the 7 nm sample, where the quantum effect is not so pronounced. As the thickness reduces down to 2.5 nm, clear discrepancy can be seen between the Drude model and experiment. Also, it is found that the ultra-thin gold film has quite weak nonlocal effect, and the nonlocal calculation shows negligible difference as compared to Drude model. For the quantum size model, good prediction has been found at long wavelength region ($\lambda > 1.4\ \mu$m), but considerable disagreement shows up at shorter wavelength for 2.5 nm thin film. Instead, our QEM has

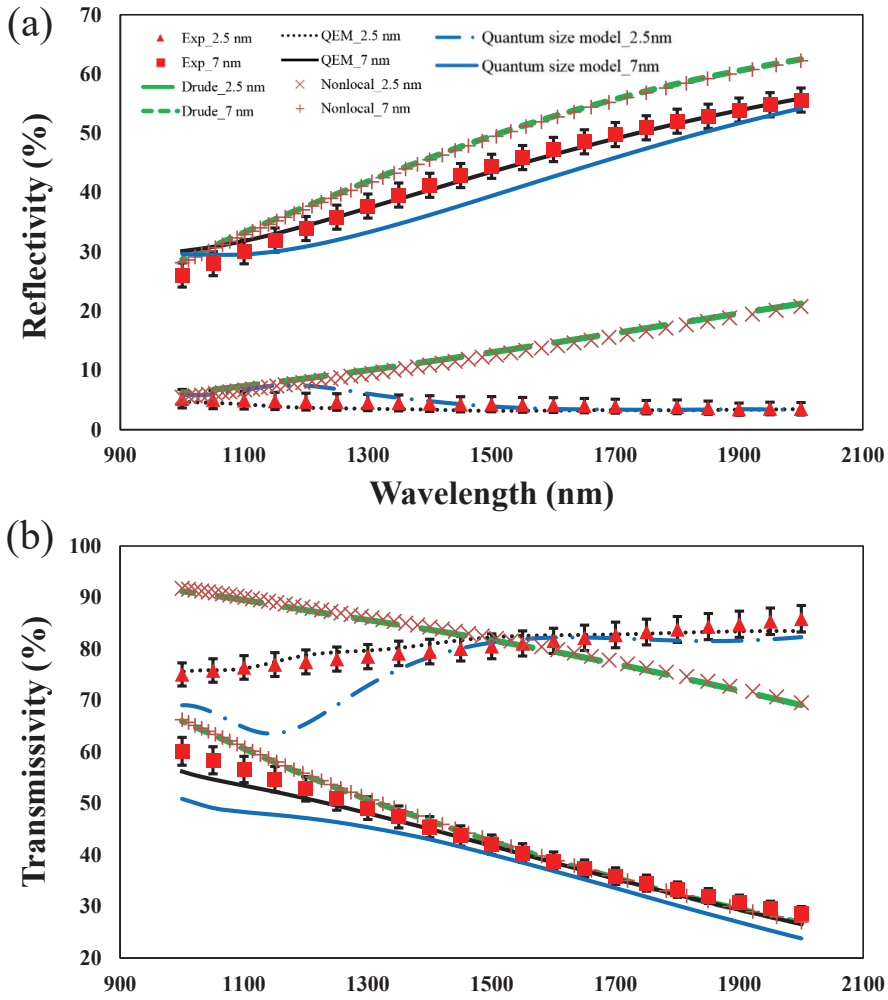

Figure 2.4: Comparison between reflection (a) and transmission (b) of which the refractive index n and k are from Drude model, nonlocal model, quantum size model, and QEM.

excellent agreement with experimental results for both 7 nm and 2.5 nm samples in a broad range of wavelength. Figure 2.4 clearly implies that QEM, which considers the quantum confinement effect together with the impact of self-consistent electron redistribution, should be used for the case of metal quantum well structures.

2.3 Nonlinear material properties with quantum size effect

With the size of plasmonic devices entering into the nanoscale region, the impact of quantum physics needs to be considered. In the previous section, we proposed the QEM to describe the linear permittivity of the plasmonic material in quantum region. Besides the linear permittivity, there exist the high order susceptibilities for the plasmonic materials that would draw much more attention, due to the high demand for such a material that efficient light-matter interaction can happen. However, for the efficient plasmonic nonlinear medium, there haven't been explored much so far. As we know that, the nonlinear susceptibilities of bulk plasmonic materials, such as Au or Ag, is relatively small [52], which limit the practical application in integrated nonlinear optical devices. On the other hand, the giant electrical field enhancement and the ability to confine the light into ultra-small volume owned by the plasmonics are the crucial factors for the efficient nonlinear interactions. Thus, engineering the nonlinear properties of the plasmonic materials in quantum region would have great interests with fruitful underlying physics and vast potential applications in nanophotonics and nonlinear optics. In this section, we would like to follow the quantum description of the metallic quantum well, and extend it into the nonlinear susceptibilities region.

The physical reasons for high nonlinear response from the metallic quantum wells are the quantum size effect and the high free electron density in the metal. According to the quantum nonlinear theory [53], the third order nonlinear susceptibility is proportional to $N(\mu_{mn})^4/(\omega_{mn} - \omega - i\gamma_{mn})^3$, where N is the density of free electrons, $\mu_{mn} = -e\langle m|\hat{r}|n\rangle$ is the dipole moment associated with the transition between state n and m. The denominator is related to the resonant transition, and γ_{mn} is a damping term. The magnitude of $\chi^{(3)}$ is mainly determined by N and μ_{mn}. Due to the quantum confinement effect, free electrons in the metal are quantized into subbands where their wave functions in the quantum well direction have an extension that is comparable to the well width ($\sim$several nm). The dipole moment associated to these intersubband transitions are

on the order of $e \cdot nm$, which is much larger than those of the traditional nonlinear crystals. On the other hand, the N of a typical plasmonic materials, such as Au or Ag, is on the order of $10^{28} m^{-3}$, much higher than that of a semiconductor quantum well. These two facts imply that the nonlinear response of a metallic quantum well would be much larger than that of traditional nonlinear crystals and semiconductor quantum wells, making it among the most promising material systems for nonlinear applications.

After solving the eigen states and functions using the QEM described in the sectinon 2, the second and third nonlinear susceptibility can be express as follows:

$$\begin{aligned}
\chi^{(2)}_{ijk}(\omega_p+\omega_q,\omega_q,\omega_p) = \frac{N}{2\varepsilon_o\hbar^2}\sum_{lmn}(\rho^{(0)}_{ll}-\rho^{(0)}_{mm}) \\
\times \frac{\mu^i_{ln}\mu^j_{nm}\mu^k_{ml}}{[(\omega_{nl}-\omega_p-\omega_q)-i\gamma_{nl}][(\omega_{ml}-\omega_p)-i\gamma_{ml}]} \\
+ \frac{\mu^i_{ln}\mu^k_{nm}\mu^j_{ml}}{[(\omega_{nl}-\omega_p-\omega_q)-i\gamma_{nl}][(\omega_{ml}-\omega_q)-i\gamma_{ml}]} \\
+ \frac{\mu^j_{ln}\mu^i_{nm}\mu^k_{ml}}{[(\omega_{nm}+\omega_p+\omega_q)+i\gamma_{nm}][(\omega_{ml}-\omega_p)-i\gamma_{ml}]} \\
+ \frac{\mu^k_{ln}\mu^i_{nm}\mu^j_{ml}}{[(\omega_{nm}+\omega_p+\omega_q)+i\gamma_{nm}][(\omega_{ml}-\omega_q)-i\gamma_{ml}]}
\end{aligned} \tag{2.6}$$

$$\begin{aligned}
\chi^{(3)}_{kjih}((\omega_1+\omega_2+\omega_3,\omega_1,\omega_2,\omega_3)) = \frac{N}{\varepsilon_o\hbar^3}P_I\sum_{nmpl} \\
\times\{\frac{[\rho^{(0)}_{mm}-\rho^{(0)}_{ll}]\mu^k_{mn}\mu^j_{np}\mu^i_{pl}\mu^h_{lm}}{[\omega_{nm}-\omega_1-\omega_2-\omega_3-i\gamma_{nm}][\omega_{pm}-\omega_1-\omega_2-i\gamma_{pm}][\omega_{lm}-\omega_1-i\gamma_{lm}]} \\
-\frac{[\rho^{(0)}_{ll}-\rho^{(0)}_{pp}]\mu^k_{mn}\mu^j_{np}\mu^i_{lm}\mu^h_{pl}}{[\omega_{nm}-\omega_1-\omega_2-\omega_3-i\gamma_{nm}][\omega_{pm}-\omega_1-\omega_2-i\gamma_{pm}][\omega_{pl}-\omega_1-i\gamma_{pl}]} \\
+\frac{[\rho^{(0)}_{ll}-\rho^{(0)}_{nn}]\mu^k_{mn}\mu^j_{pm}\mu^i_{lp}\mu^h_{nl}}{[\omega_{nm}-\omega_1-\omega_2-\omega_3-i\gamma_{nm}][\omega_{np}-\omega_1-\omega_2-i\gamma_{np}][\omega_{nl}-\omega_1-i\gamma_{nl}]} \\
-\frac{[\rho^{(0)}_{pp}-\rho^{(0)}_{ll}]\mu^k_{mn}\mu^j_{pm}\mu^i_{nl}\mu^h_{lp}}{[\omega_{nm}-\omega_1-\omega_2-\omega_3-i\gamma_{nm}][\omega_{np}-\omega_1-\omega_2-i\gamma_{np}][\omega_{lp}-\omega_1-i\gamma_{lp}]}\}
\end{aligned} \tag{2.7}$$

where the $\rho_{ll} - \rho_{mm}$ represents the population difference and P_I is the denotes the intrinsic permutation operator. As we shown before (Fig. 1.4), the metallic quantum well formed by the ultra-thin plasmonic film has the unique feature of multiple intersubband transitions in the visible/near-infrared range, which makes the engineering of the nonlinear susceptibilities from the metallic quantum well as the most promising candidate for efficient light-matter interaction, covering from the visible all the way to the infrared.

Chapter 2, in part, is a reprint of the material as it appears in Nanophotonics 4, 413-418 (2015), Haoliang Qian, Yuzhe Xiao, Dominic Lepage, Li Chen, Zhaowei Liu. The dissertation author was the primary investigator and author of this paper.

Chapter 3

Engineering of the optical nonlinearity in quantum region

With the developed theoretical modeling (QEM) and the high-efficiency nonlinearities predicted in the metallic quantum well system in Chapter 2, we would like to describe in details for the experimental realization of the nonlinearities, including the second and third optical nonlinearites in this chapter. As we mentioned before, the huge free-electron density and the large transition moment are the two key factors that boost the nonlinear coefficient. Besides that, the large number of intersubband in the visible/near-infrared range and easy-to-tune of the quantized wavefunctions make the metallic quantum well unique for the investigation of the efficient nonlinear light-matter interactions. In the following sections, we would introduce a coupled metallic quantum wells for the second order susceptibility (SHG) and a regular metallic quantum well for the third order susceptibility (Kerr).

3.1 Large second order nonlinearity from coupled metallic quantum wells

New materials that exhibit strong second-order optical nonlinearities at a desired working frequency are of paramount importance for nonlinear optics. Giant second-order susceptibility $\chi^{(2)}$ has been obtained in semiconductor quantum wells (QWs) [54–58]. Unfortunately, the limited confining potential in semiconductor QWs causes formidable challenges to scale such a scheme into the visible/near-infrared (NIR) frequencies for more vital nonlinear-optics applications. As we mentioned in the Chapter 2, the metalic quantum well could be used to enable the high nonlinear coefficient in the visible/NIR range due to the large depth of these QWs. And the second order coefficient can be further enhanced by the coupled metallic quantum wells to break the symmetry and provide the double transitions. Recent advances in ultrathin gold films introduce a possible solution, however, restricted by the accessible growth technologies, these ultrathin gold films cannot be used for sophisticated coupled QW heterostructures as the epitaxial semiconductor wells.

In a different context, transition metal nitrides have been the subject of much recent attention for their use in plasmonics [59, 60]. These plasmonic materials have optical responses similar to those of gold while showing vastly enhanced chemical and thermal stability [28, 61], rendering them suitable for the study of optical nonlinearities. Among them, titanium nitride (TiN) can exist in a range of non-stoichiometric compositions, and can be grown epitaxially on various transparent substrates such as sapphire [62, 63]. Epitaxial heterostructures of TiN/Al_2O_3 have therefore become an excellent candidate to design the ultra large $\chi^{(2)}$ in the frequency range covering from visible to NIR spectra.

Here, in this section, we would like to introduce a coupled metal/dielectric heterostructured platform (TiN/Al_2O_3 epitaxial layers), to demonstrate an extremely high $\chi^{(2)}$ of around 1500

pm/V at NIR frequencies. It is composed of two metallic quantum wells separated by 0.5 nm Al_2O_3, to form the coupled metallic quantum well (cMWQ). And by combining the aforementioned heterostructure with the large electric field enhancement afforded by a nanostructured metasurface, the power efficiency of second harmonic generation (SHG) has achieved 10^{-4} at an incident pulse intensity of 10 GW/cm^2, representing several orders of magnitude improvement compared to previous demonstrations from nonlinear surfaces at similar frequencies [19, 64, 65].

The demonstrated high $\chi^{(2)}$ is more than an order higher than those of traditional nonlinear crystals, and a few orders higher than those of classic plasmonic films. The physical reasons are provided as follows. The cMQWs were delicately designed to support three electronic subbands with constant energy spacing (i.e. $E_iE_{i-1} = E_{i+1}E_i = \hbar\Omega$, where $\hbar$ is the reduced Plank constant and Ω is the double transition frequency), such that $\chi^{(2)}$ near the double transition frequency Ω reads

$$\chi^{(2)}(\omega) = \frac{n_{i-1} - n_i}{\hbar^2 \varepsilon_0} \frac{e^3 z_{i-1,i} z_{i,i+1} z_{i+1,i-1}}{(\omega - \Omega - i\Gamma_{i,i-1})(2\omega - 2\Omega - i\Gamma_{i+1,i-1})} \tag{3.1}$$

Above, n_i, ε_0, and e are the electron density in the i_{th} subband, the vacuum permittivity, and the electron charge, respectively. The dipole moment $ez_{i,j}$ and the decay rate $\Gamma_{i,j}$ are associated with optically active subbands. Only the lowest of the three electronic subbands E_{i-1} was assigned below the Fermi level E_F in order to increase the electron density of $(n_{i-1}n_i)$ and thus the $\chi^{(2)}$. The product of the dipole moments $e^3 z_{i-1,i} z_{i,i+1} z_{i+1,i-1}$ is large in this asymmetric QWs, contributing to a large $\chi^{(2)}$ as well. In addition, a significantly enhanced $\chi^{(2)}$ is exhibited in the cMQWs when the incident frequency ω is resonant with the double transition frequency Ω. Therefore, due to the large dipole moment and the high carrier concentration within a single QW, and the double resonant transition between equally spaced electronic bound states formed by the coupled QWs, a giant $\chi^{(2)}$ in the visible/NIR range of the spectrum is expected in these proposed cMQWs.

Based on the above principle, a single cMQW unit consists of two TiN metallic wells of different thickness, separated by an ultrathin Al_2O_3 dielectric barrier, as shown in Fig. 3.1. The

widths of these wells (1.0 nm and 2.2 nm) were chosen to have a double transition frequency Ω at 920 nm and the barrier (0.5 nm) is selected to have reasonable coupling efficiency between the two metallic quantum wells using the quantum electrostatic model described in the Chapter 2, in order to produce a SHG output at the visible frequency of 460 nm (2Ω). The TiN/Al_2O_3 cMQWs were fabricated via an epitaxial growth method. Figure 3.1(b) shows a transmission electron microscope (TEM) cross-section of one sample consisting of four cMQW units, where the units are clearly visible and well-grown with a large-area uniformity. A dark-field high-resolution TEM (HRTEM) image of one cMQW unit is given in the inset of Fig. 3.1(b), showing atomic level accuracy in the thickness of both the metallic and dielectric epitaxial films. Having such high-quality metal/dielectric epitaxial heterostructures as the material platform of our cMQWs ensures precise control of intersubband quantum engineering for extremely high optical nonlinearities at visible/NIR frequencies.

Due to the polarization selection rule of intersubband transitions in a planar QW structure, only the electric field component E_z of the pump light contributes to the optical responses of the QW including the SHG. Therefore, an in-plane polarized pump light (i.e. the polarization angle $\varphi = 90^\circ$ is obliquely incident on the sample surface with a fixed incident angle of $\theta = 30^\circ$, as illustrated in the left inset of Fig. 3.2(a). Here, samples with a single cMQW unit are investigated to verify the origin of SHG. Figure 3.2(a) shows a measured emission spectrum reflected from such a sample as excited by a 920-nm (Ω) light pulse with an average power of 3 mW. As can be clearly seen, the spectrum features a sharp peak centered at the SHG wavelength of 460 nm (2Ω). The measured dependence of the total (transmitted and reflected) SHG emission intensity on the incident power is shown in the right inset of Fig. 3.2(a), which agrees well with the quadratic prediction [53].

In general, phase matching is a critical requirement for a SHG nonlinear optical process. However, because the propagation distance (less than 10 nm for the single cMQW unit) is significantly shorter than the SHG coherence length, the phase-matching condition is automatically

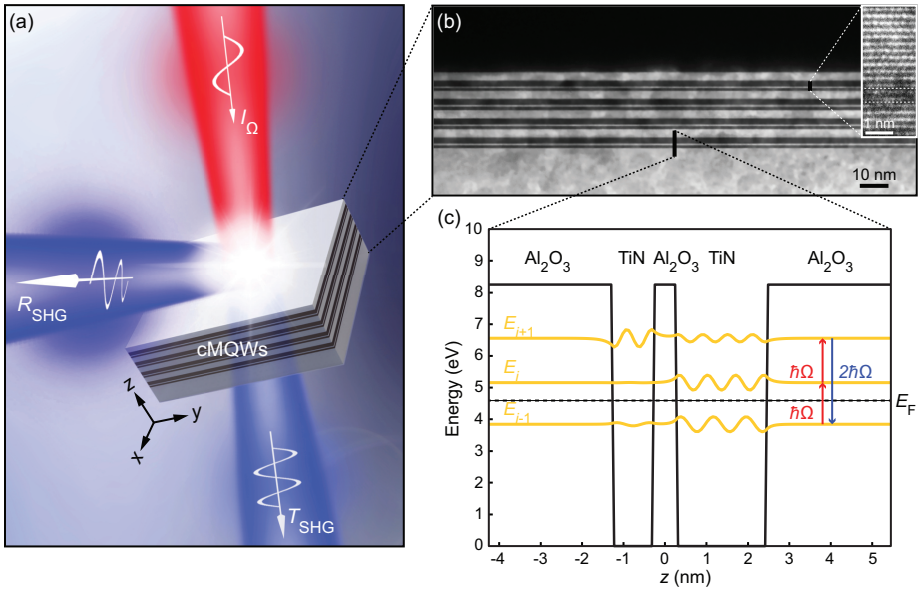

Figure 3.1: cMQWs for extreme optical nonlinearities and high efficient visible-frequency SHG. (a) Schematic illustrating how incident light I_Ω is converted into the reflected R_{SHG} and transmitted T_{SHG} SHG waves by the cMQWs based ultrathin film where phase matching is automatically satisfied. (b) TEM cross-section of such an ultrathin film system with four units of the cMQWs. Inset shows its dark-field HRTEM image where atomic-level epitaxial layers are clearly visible. (c) Conduction band diagram of a single cMQW unit. The electron wave-functions (yellow lines) of three subbands near the Fermi level E_F (∼4.6 eV) are plotted. These subbands are designed to provide a double resonant transition $(\hbar\Omega)$, which gives rise to the desired SHG $(2\hbar\Omega)$ at the visible frequency.

satisfied in this cMQW system. In order to determine the directionality of the SHG emission, a charge-coupled device (CCD) at the back-aperture plane of the collection objective is used to measure the emission signal. The measurement setup is schematically provided in Fig. 3.3. Figure 3.2(b) shows the back-aperture images at four different incident polarization states from the out-of-plane (with respect to the incident plane, $\phi = 0°$) to the in-plane ($\phi = 90°$), with fixed incident angle of $\theta = 30°$. It can be clearly seen that the SHG signals exhibit a sharp peak localized at the collection angle of $\theta = 30°$ in the back-aperture plane. This proves that the SHG signals are coherently generated by the incident light (not a photoluminescence process), as illustrated in Fig. 3.1(a). In addition, the emission intensity has a $sin^4(\phi)$ dependence, which originates from the polarization selection rule of intersubband transition in QW structures [66].

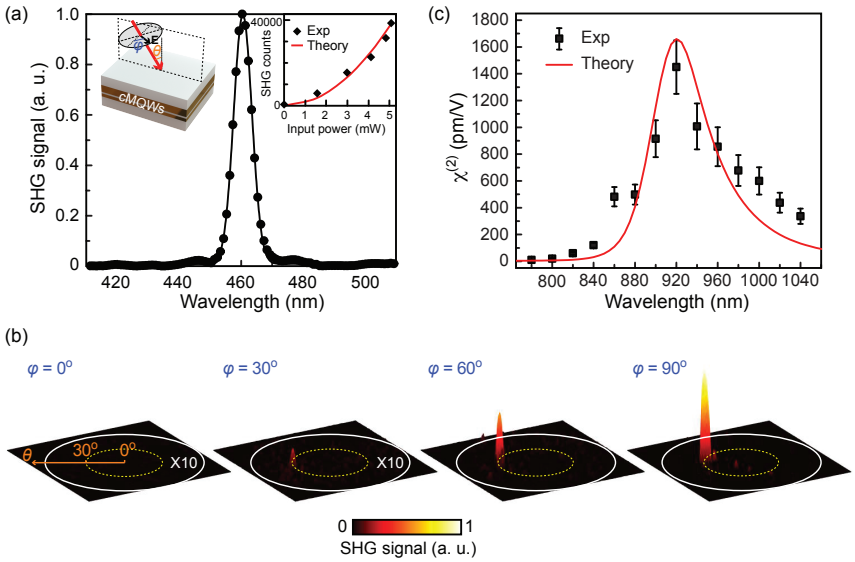

Figure 3.2: Experimental characterization of SHG enabled by cMQWs. (a) SHG emission spectrum under a 920-nm light pulse (100 fs, 80 MHz) excitation with an average power of 3 mW. Solid black circles are the experimental result which is fitted by a Gaussian lineshape function (black line). Left inset shows the experimental configuration where the pump light (thick red arrow) with the electric field E (black arrow) polarized at angle to the out-of-plane (with respect to the incident plane) direction is obliquely incident on the sample surface with the incident angle θ. Right inset shows the total (transmitted and reflected) SHG emission at various incident powers. The experimental results fall on the quadratic theoretical curve. (b) CCD images at the objectives back-aperture plane (equivalent to the Fourier plane) showing the evolution of emissions at 460 nm as the polarization angle φ and thus E_z increases. The dashed yellow circle highlights the collection angle of $\theta = 30°$, while the solid white circle indicates the maximum collection angle of the objective. (c) Wavelength dependence of $\chi^{(2)}$ for a single unit of the cMQWs. The presence of a resonant peak for the wavelength-dependent $\chi^{(2)}$ evidences the double resonant transition in the single cMQW unit.

The giant $\chi^{(2)}$ for visible-frequency SHG enabled by cMQWs relies on the double resonant transition. Figure 3.2(c) shows the experimentally obtained $\chi^{(2)}$, compared with the theoretical prediction from Eq. 3.1. This $\chi^{(2)}$ spectrum has a resonant peak centered at the double transition frequency Ω (920 nm) as we designed in Fig. 3.1(c), indicating again the intersubband resonant transition for the cMQWs. The $\chi^{(2)}$ achieves up to 1500 pm/V at the NIR frequency, a value more than 20 times higher than those of traditional nonlinear crystals (75 pm/V for $LiNbO_3$) and several orders higher than those of typical metallic structures (∼1 pm/V) [67]. Such a large $\chi^{(2)}$

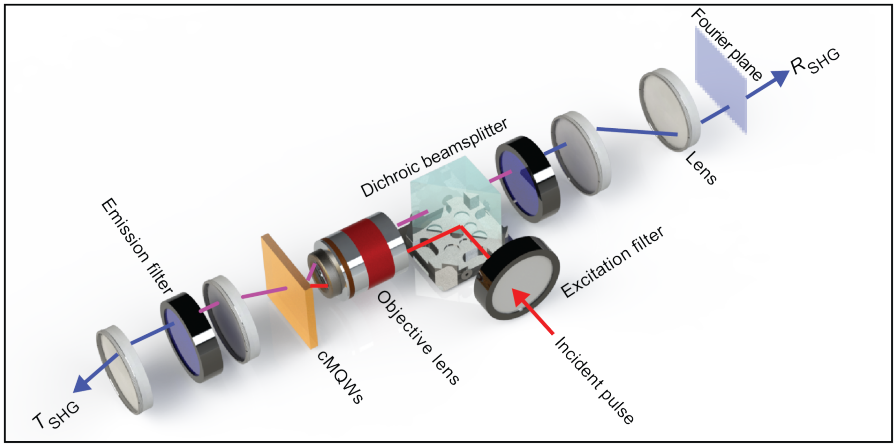

Figure 3.3: Experimental setup for the SHG measurement. Laser pulses with a 100-fs pulse width and an 80-MHz repetition rate were incident to excite the SHG. A 50X objective lens (NA = 0.8, Olympus IX81) was used to focus the incident pulse and collect the reflected waves. The incident power of the pulse laser was measured by a power meter (Vega), while the excited SHG emission power was collected at both the transmission and reflection sides by a photon counting detector (Horiba PPD). The angle distribution of the SHG emission was obtained at the Fourier plane with a charge coupled device (Andor iXon EMCCD), and the results are present in Fig. 3.2

at NIR frequency shows that the cMQWs are an excellent candidate for ultra-compact nonlinear components.

Due to the exceptional thermal stability from the TiN/Al_2O_3, the cMQW system can operate at relatively high intensity. In Fig. 3.4, power dependent SHG measurement is performed and all the output SHG power forms the quadratic relations and the power efficiency ($P_{\mathrm{SHG}}/P_{\mathrm{FF}}$) lies on a linear line, which indicates the remarkable $\chi^{(2)}$ from the cMQW system.

Plasmonically-enabled electric field enhancements have recently been used to overcome the diffraction-limited dimensions, leading to ultracompact nonlinear optoelectronic devices. Now, we combine the plasmonic enhancement with the ultra large $\chi^{(2)}$ for enhanced surface SHG at the visible frequency. It is done by constructing cMQWs-embedded metasurface on which the local electric fields are enhanced, due to two plasmonic resonances at both the double transition frequency Ω (920 nm) and the SHG frequency 2Ω (460 nm). As such, the absorption of photons at the fundamental frequency Ω in cMQWs will be enhanced by the first plasmonic resonance,

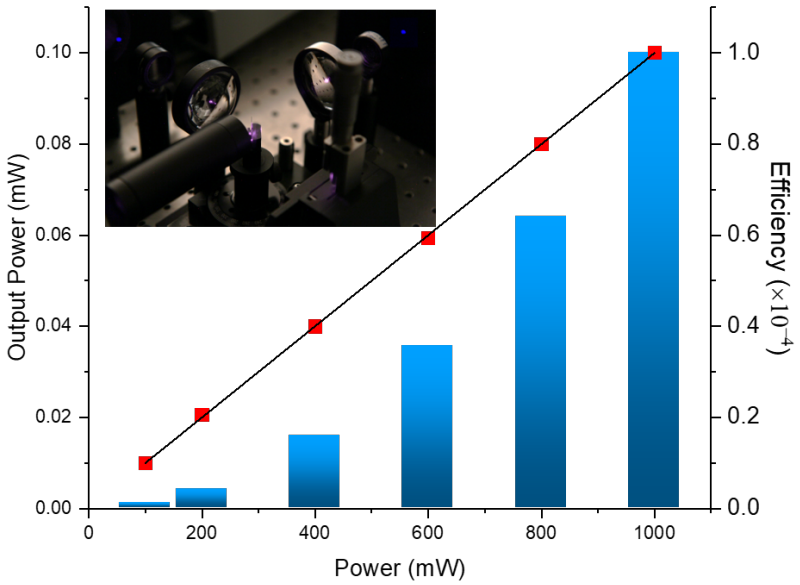

Figure 3.4: Power dependent SHG measurement on 4 units of cMQWs. Here, the incident laser pulse was focused by a lens onto the sample that was rotated 45° with respect to the incident beam. The power efficiency reaches 10^{-4} when the incident power is 1000 mW (160 GW/cm^2 correspondingly). It is so high so that distinct SHG signals along both the transmitted and reflected directions are clearly visible.

while the radiative decay of the cMQWs at the SHG frequency 2Ω will be boosted by the other plasmonic resonance, leading to an efficient SHG. Such metasurfaces also give rise to efficient conversion of the impinging transverse electric field polarization into the desired z-direction [68], enabling normal excitation of the incident beam to expand the usability of the extremely high nonlinear cMQWs. In Figure 3.5, the z-component of the electrical field distributions were plotted, where one can see that the optical resonance at the fundamental wavelength results from the metal-insulator-metal plasmonic waveguide-like confinement, while the SHG wavelength optical resonance arises owing to the localized surface plasmon supported by the silver nanocube array.

Figure 3.6(a) depicts the designed metasurface structure, which, from top to bottom, is composed of, an array of monocrystalline silver nanocubes (110-nm edge length, Fig. 3.6(b)),

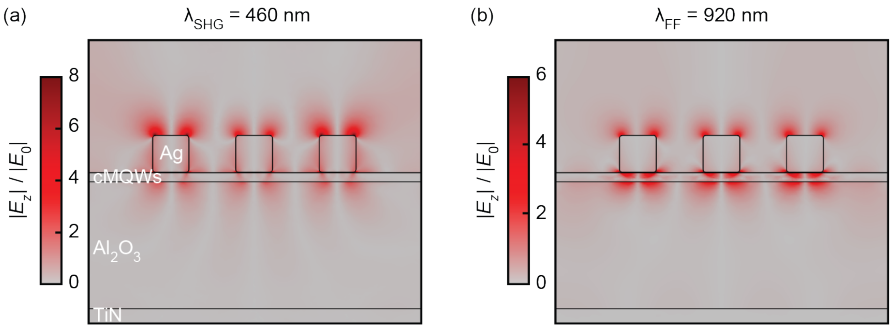

Figure 3.5: Simulated electrical field ($|E_z|/|E_0|$) distributions for the SHG (a) and fundamental (b) wavelengths. Here, $|E_0|$ is the amplitude of the incident electrical field.

4 units of cMQWs, a single layer of Al_2O_3 (380 nm thick), and a 50-nm TiN layer. The array of monocrystalline silver nanocubes was self-assembled and then transferred on top of the epitaxial TiN/Al_2O_3 multilayer, and a characteristic SEM image is given in Fig. 3.6(b). These homogenously distributed high-quality monocrystalline silver nanocubes (see the HRTEM images in the insets of Fig. 3.6(b)) are suitable to enhance the light field by plasmonic resonances [10,69].

Figure 3.6(c) shows the measured scattering and absorption spectra. The resonant peak centered at Ω in the absorption spectrum indicates the desired fundamental-frequency absorption enhancement, while the dominant resonant peak centered at 2Ω in the scattering spectrum reveals a high out-coupling efficiency at the SHG wavelength. It is thus expected that there would be a massive enhancement of the visible-frequency SHG efficiency. The emission spectrum of the cMQWs-embedded metasurface, as excited by a light beam of normal incidence (Fig. 3.6(a)), shows a well-behaved visible-frequency SHG. Figure 3.6(d) gives the corresponding power efficiency $P_{\mathrm{SHG}}/P_{\mathrm{FF}}$, where P_{SHG} (P_{FF}) is the average power at the SHG (fundamental) wavelength; it reaches 10^{-4}, more than four orders higher than those of the previous demonstrations of plasmonically-enhanced SHG at the visible/NIR wavelength [16,19,64,65,70]. All crystalline materials and specifically-designed electronic and photonic engineering are attributed to the giant visible-frequency SHG power efficiency, which enables this optical metasurface to be used in ultracompact nonlinear devices in an on-chip integrative manner.

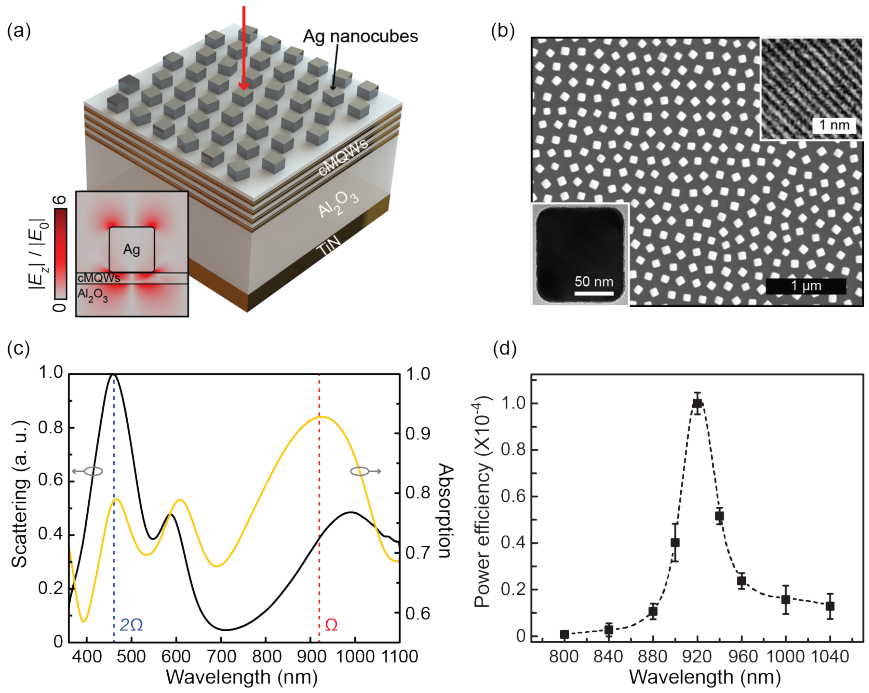

Figure 3.6: Efficient visible-frequency SHG from cMQWs-embedded monocrystalline silver nanocube metasurface. (a) Schematic of the high SHG efficiency metasurface excited by a normal incidence pump light (thick red arrow). Inset shows the simulated electric field enhancement on the embedded cMQWs. (b) SEM image of the top silver nanocube array. Bottom left inset is a TEM image of a single silver nanocube, while top right inset shows its HRTEM image where its crystalline lattice can be clearly seen. (c) Measured scattering (black line) and absorption (yellow line) spectra. Two vertical dashed lines indicate the SHG wavelength (2Ω) and the corresponding fundamental wavelength (Ω), respectively. (d) Wavelength dependence of the power efficiency at the incident pulse intensity of 10 GW/cm^2. Solid black squares are the experimental result, while the black dashed line is the spline-fitted curve. The visible-frequency SHG power efficiency reaches 10^{-4}.

To summarize this section, we have shown a new coupled-metallic quantum well based material system that exhibits an extremely high $\chi^{(2)}$ at the NIR frequency and demonstrated a giant visible-frequency SHG power efficiency in such a cMQWs-embedded metasurface. Further integration of more advanced configurations includes the broadband efficient SHG by stacking cMQW ultrathin films with different double transition frequencies. Likewise, combinations of optical nonlinearities, e.g., both a high $\chi^{(2)}$ and a large $\chi^{(3)}$, would be conceivable in a single material system in a concise manner. Nanostructured materials with such giant SHG power

efficiency are expected to enable new on-chip surface nonlinear optical applications.

3.2 Giant third order nonlinearity from metallic quantum wells

With the large $\chi^{(2)}$ demonstrated in the coupled metallic quantum well system, the high $\chi^{(3)}$ from the metallic quantum well is also expected. Unlike the symmetry-broken requirement for the second order susceptibility, the third order nonlinear can be realized in just one metallic quantum well. In this section, we would discuss about the third order nonlinearity in details, including the underlying physics, device fabrication and characterization, and the potential applications.

The third order nonlinearity, especially the Kerr effect, is one of the most prominent nonlinear susceptibilities. The Kerr effect leads to a large number of practical applications, such as the wave mixing [71,72], broadband light generation [26,27], frequency comb generation [21,73] and so on. In additional, the frequency-comb generated in optical cavities has been applied in metrology optical communication system, and super-continuum generated through photonic crystal fibers are nowadays routinely used as a coherent broadband light source in imaging. However, despite much effort and many years of advancement in this field, chip-scale-integrated nonlinear optics has yet to be realized due to the lack of materials with exceptionally high nonlinear responses. Here, we studied the optical Kerr nonlinear properties on a metallic quantum well (MQW) formed by a layer of 3 nm gold film, and demonstrated that the quantum size effect can lead to giant nonlinear response, which shows a several-order enhancement compared with traditional nonlinear materials, making the thin metallic quantum well promising for the on-chip-integrated nonlinear applications.

Figure 3.7(a) shows a transmission electron microscopy (TEM) image of the cross-section for the 3 nm metallic quantum well samples. The confinement of the free electrons of gold is

realized by the large band gap of the two oxide materials (Al_2O_3 and SiO_2). As shown in the zoomed-in view of the TEM image (Fig. 3.7(b)), the gold film is continuous at the thickness of 3 nm. Although TEM figure can accurately tell us the thickness information of the MQW, atomic force microscopy (AFM) measurement is used to obtain the surface roughness right after the Au film deposition. Figure 3.7(c) shows the statistics of the film thickness variations through the AFM measurement, where we can see the surface roughness (root mean square) is about ± 0.25 nm.

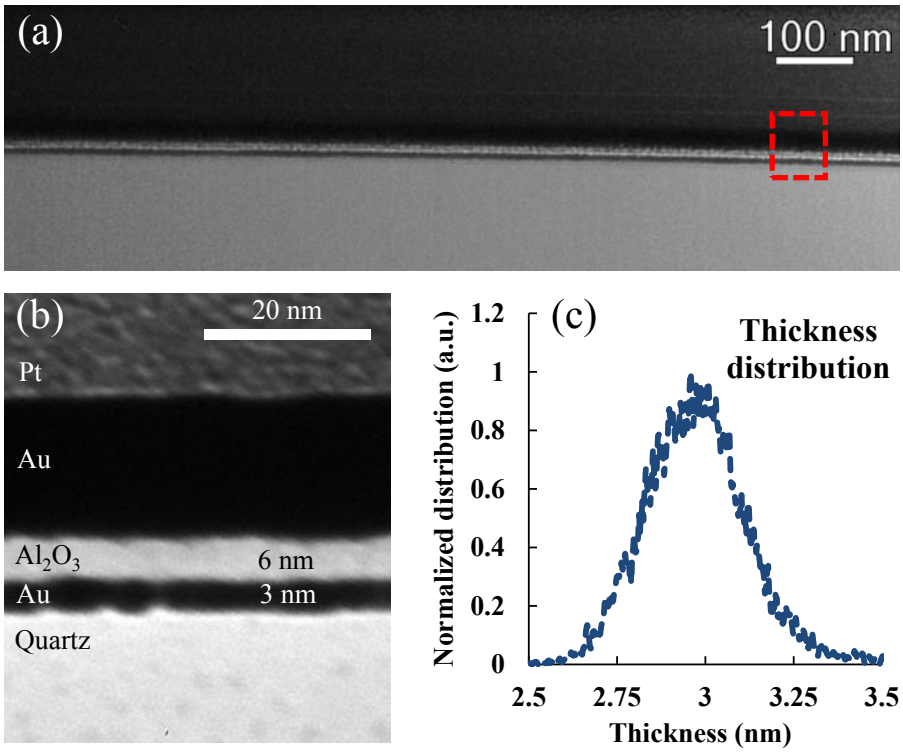

Figure 3.7: Sample characterization for the Au metallic quantum well. (a) Cross-sectional TEM image of the MQW sample prepared by focused ion beam (FIB). (b) A zoomed-in view of the MQW, that is, the bottom Au layer, indicates that the gold film is continuous. The thick Au and Pt layers atop were only used to facilitate the FIB process. (c) Statistics of the film thickness variations obtained from AFM measurement right after 3 nm gold film growth on the quartz substrate but before the (Al_2O_3 film deposition. The surface roughness is around ± 0.25 nm.

To characterize the nonlinear optical properties of the MQW, z-scan experiment is performed (the schematic setup is shown in Fig. 3.8(a)). Z-scan measurement is a sensitive and simple technique for measuring the complex nonlinear refractive index of a material [74].

Closed (normalized to open) and open aperture z-scan curve of the 3 nm MQW with 900 nm incident wavelength and 111 mW incident power is depicted using red circles in Fig. 3.8(b),(d), respectively. By fitting with the standard z-scan theory [74], the Kerr coefficient is calculated to be $(3.9-0.51i)\times 10^{-9}$ cm^{2}W^{-1}. To obtain the third-order susceptibility, the refractive index n and extinction coefficient k is needed. For this purpose, reflection and transmission measurements are performed and a two dimensional Newton$'$s method together with a multilayer transmission algorithm is used to extract the n, k values (see details in the Chapter 2 section 1). With n=0.4 and k=3.7, the third order nonlinear susceptibility is calculated by

$$\chi^{(3)} = \frac{Re\{n_2\} + iIm\{n_2\}}{283} n(n+ik) \tag{3.2}$$

which gives $\chi^{(3)} = (0.49+2.0i)\times 10^{-15}$ m^{2}V^{-2}. The magnitude of this value shows a 4 order enhancement compared to the intrinsic value of bulk gold measured by four wave mixing (FWM) [75]. The measured Kerr coefficient of the 3 nm MQW is 6 to 8 orders larger than that of the traditional nonlinear mediums, such as fused silica [53]. It is worth noting that the MQW is a flat metal film, and no plasmonic mode (either localized or propagating) can be excited in the experiment. This rules out possible contributions from local field enhancement [76, 77], but purely an intrinsic response of the MQW. It also indicates that the nonlinear response of the MQW may be further boosted by combining with additional plasmonic resonance structures with large field enhancement factors. The incident power dependent nonlinear phase changes is plotted out in Fig. 3.8(c). Clearly, all data falls on a straight line crossing origin, confirming the detected nonlinear effect comes solely from the third order Kerr response.

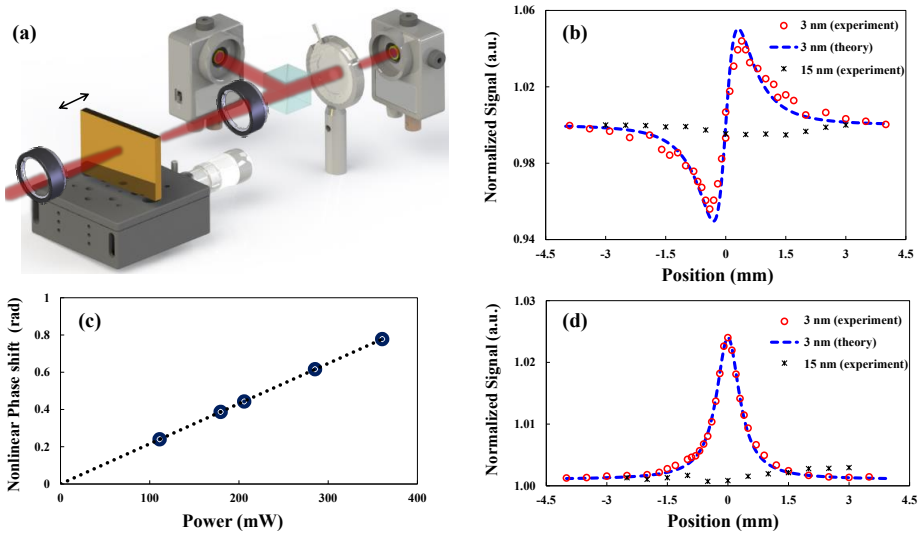

Figure 3.8: Z-scan nonlinear measurement for the Au metallic quantum well. (a) Schematic z-scan setup for third-order nonlinearity characterization. A femtosecond laser beam (Ti-sapphire laser, Mai Tai HP from Spectra-Physics, linearly polarized, 80 fs time width and 80 MHz repetition rate) is focused onto the MQW sample through a lens (f =3 cm). The raw laser beam diameter is about 3.5 mm, resulting in a Gaussian beam waist about 9 μm at the focus. The MQW is moved along the optical axis near the focus, two power metres are used to record the open and closed aperture z-scan signal through one collimation lens and a beam splitter. The closed aperture (b) and open aperture (d) z-scan curves for the 3 nm (red-circle) and 15 nm (black-cross) Au films using 900 nm incident wavelength with power of 111 and 690 mW. The closed aperture data are normalized to that of the open aperture. Z-scan signal of 3 nm sample is fitted by the standard z-scan theory (blue-dashed), from which the Kerr coefficient is extracted. (c) The measured nonlinear phase shift for different incident power. The dashed line is the mathematically linear fitting for the measurement data and nonlinear phase change is zero at zero intensity.

The physical reasons for such a giant nonlinear response are the quantum size effect and the high free electron density of the metal. As we have discussed in the Chapter 2 section 3, the magnitude of $\chi^{(3)}$ is mainly determined by density of free electrons N and the dipole transition element μ_{mn}. And with the large dipole moment from the quantized wave-functions and the intrinsic huge amount of free electrons. the MQW system proves to have pronounced Kerr response as expected, making it among the most promising material systems for nonlinear applications.

As a direct comparison and verification, z-scan measurements for a thick gold film (15

nm gold film grown on quartz substrate with 6 nm Al_2O_3 on top) are also performed with 900 nm incident wavelength and 690 mW incident laser power. For a 15 nm gold film, the impact of quantum size effect is much smaller. As shown in Fig. 3.8(b), no signal is detected at the closed aperture. For the open aperture, a change in normalized transmission T=-0.133% is recorded, which results in an imaginary part for the Kerr coefficient to be 3.4×10^{-12} cm^{2}W^{-1}. Using the literature data for the n and k for bulk gold at 900 nm (n=0.17 and k=5.72) [46], the third order nonlinear susceptibility for 15 nm gold is calculated to be $\chi^{(3)} = (-9.1 + 0.35i) \times 10^{-19}$ m^{2}V^{-2}, which agrees reasonably well with previous z-scan measurements of gold Kerr nonlinearity using femtosecond laser sources ($\leqslant$ 100 fs) [52, 78]. The measurement results are summarized and compared in Table 3.1. The $|\chi^{(3)}|$ of 15 nm gold film is slightly larger than that of the bulk gold measured by FWM [75], which might relate to the weak confinement effect [79]. The slightly larger $|\chi^{(3)}|$ from Ref. [78] using z-scan with 100 fs pulse compared with Ref. [75] could come from using a wavelength closer to the interband transition. The much larger $|\chi^{(3)}|$ reported by using 5.8 ps pulse is due to the thermal nonlinear response [78].

Table 3.1: Comparison of the $\chi^{(3)}$ values of gold from different measurements

	Measurement method	τ_{pulse}	$\lambda(nm)$	$\lvert\chi^{(3)}\rvert$(m^{2}V^{-2})
3 nm MQW	Nonlinear spectral broadening	80 fs	900	2.01×10^{-15}
Bulk [75]	Four wave mixing	200 fs	800	2×10^{-19}
3 nm MQW	z-scan	80 fs	900	2.06×10^{-15}
15 nm gold	z-scan	80 fs	900	9.1×10^{-19}
20 nm MQW [78]	z-scan	100 fs	630	7.69×10^{-19}
20 nm MQW [78]	z-scan	5.8 ps	630	7.58×10^{-17}

The nonlinear response of the MQW is related to the transition of the quantized free electrons between the subbands, which is determined by the MQW geometry. To explore this feature, z-scan experiment is performed on the 3 nm MQW by scanning the wavelength from 690 nm to 1020 nm. The measured nonlinear coefficients, both the real and imaginary parts, are plotted using red and green dots respectively in Fig. 3.9(a). The measured nonlinear indices of the 3 nm MQW clearly show two resonance peaks in the measured spectral range, near 740 nm

and 900 nm respectively.

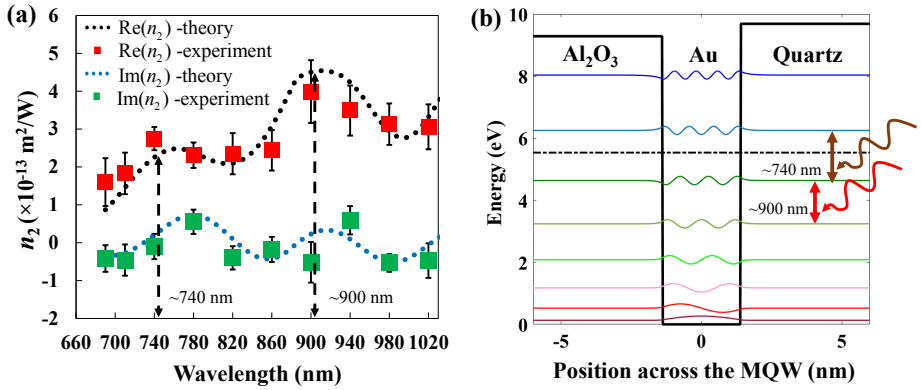

Figure 3.9: Wavelength dependence of the Kerr coefficient. (a) Real (red-dots) and imaginary (green dots) parts of the nonlinear indices measured for the 3 nm MQW as a function of incident laser wavelength. The fluctuations in multiple measurements at various locations are indicated by the error bars (standard deviation). Two resonance peaks are found near 740 nm and 900 nm, respectively. Theoretical predictions (black and blue dotted lines) agree well with experimental results. (b) Calculated quantized energy states and their corresponding wave functions from the self-consistent calculation of the Schrödinger and Poisson equations. For the 3 nm quantum well, the dipole dephasing time, which relates to the damping rate as $\tau = 1/\gamma$, is 7.5 fs and the effective mass of the electron is $0.35 \times m_e$, where m_e is the free electron mass. The Fermi energy level is plotted by dash-dotted black line. The transitions responsible for the two resonances observed in (a) are marked as the arrows in this figure as well.

In order to fully understand the nonlinear optical properties of the MQW, we also adopt the quantum electrostatic model that is based on the self-consistent solution from Schrödinger and Poisson equations, which has been described in Chapter 2. As shown in Fig. 3.9(b), there are 8 quantized states supported by this MQW. More specifically, we found that the transitions of the 5th to 6th and 6th to 7th eigen-energy states correspond to the experimentally observed resonant peaks around 900 nm and 740 nm, respectively. After that, a standard approach that is based on perturbation theory is adopted to calculate the $\chi^{(3)}$ of the MQW [53]. Variations in the film thickness would lead to the broadening of the resonance feature of the material response. To take this effect into account, a Gaussian-broadening approach is adopted by using the thickness variation data obtained from AFM measurement. Finally, the calculated Kerr coefficients (both the real part and imaginary part) are plotted using dotted-line curves in Fig. 3.9(a), which agree

well with the experimental results.

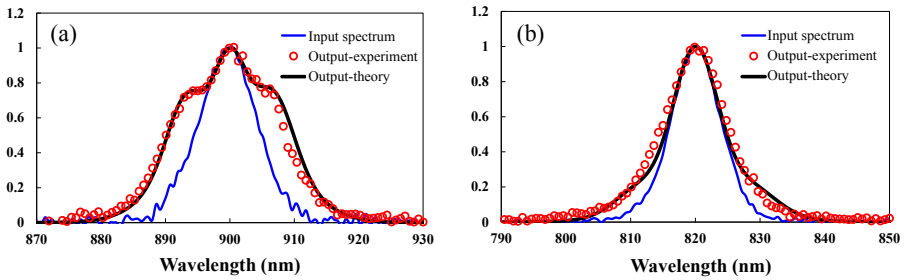

Figure 3.10: Nonlinear spectral broadening from the 3 nm Au metallic quantum well. A similar setup as the z-scan measurement is used with the sample placed at the focus for spectral broadening measurement, and the power meter at the open aperture branch is replaced by an optical spectrometer. Spectrum of an optical pulse (open red circles) measured after passing through the 3 nm MQW for incident wavelength at 900 nm (a) and 820 nm (b) using incident power of 650 mW and 750 mW. In the case of 820 nm, the SPM-induced spectral broadening can only be seen at the spectral wings, and the nonlinear phase shift is estimated to be 0.6π. In the case of 900 nm, where the Kerr coefficient is at a resonance peak, the SPM-induced spectral broadening is much more obvious, and the nonlinear phase shift is estimated to be 0.88π. The input spectrum is shown by blue solid curves. Theoretical calculations of the transmitted spectrum based on the experimental value of n_2 measured from z-scan is plotted using black solid curves, which show excellent agreement with experimental data.

Thermal effect can play a very important role in z-scan experiment [80]. The Kerr coefficient of gold film has been reported as high as 10^{-8} $\mathrm{cm^2W^{-1}}$ previously using z-scan method [81, 82], where pulses with ps or even ns duration were used. For such long pulse width, the dominant nonlinearity is the thermal effect [83, 84]. Two kinds of thermal effect need to be considered in the case of using pulse laser with certain pulse width and repetition rate. The first one is the thermal effect within a single pulse envelope where the thermal effect is induced by the laser pulse itself when the hot electron relaxed through electron-electron and electron-phonon interaction. The other effect is the accumulated thermal effect, which becomes critical for a pulsed laser with high repetition rate. For the first case, as shown by previous pump-probe experiments [85] and the two temperature model [83], the typical hot-electron delay time for gold is about 500 fs, which is much longer than the laser pulse width (80 fs) used in this study. Therefore, the impact of hot electron effect can be safely neglected in our experiment. The second

source of thermal contribution comes from accumulated effect from the pulse train, which can be ruled out by the spectral broadening measurement. The difference in z-scan and spectral broadening measurement is that the former measures the spatial intensity dependence of the refractive index, while the latter measures the temporal intensity dependence of refractive index. In the case of z-scan, the accumulated thermal effect may lead to a spatially-dependent refractive index change because of the invariant laser intensity profile. Therefore, this type of thermal effects (which mainly comes from the contribution of the repetitive pulse train) can express similar instantaneous Kerr response (which only comes from the single pulse itself). While a stabilized accumulated thermal effect due to the repetitive pulse train is constant in the temporal domain and is independent on the each pulse shape. In this case, the accumulated thermal effect cannot contribute to the spectral broadening.

To further exclude other contributions from thermal nonlinearity, the measurement of spectral broadening of a pulse due to self-phase modulation (SPM) is performed, as shown in Fig. 3.10. The reason is that optical Kerr response is an instantaneous response, while athermal and thermal effects are much slower than Kerr response and would not lead to spectral broadening. The SPM-induced spectral broadening effect is proportional to the nonlinear phase $Re(n_2) \times I \times k \times L_{eff}$, where I is the light intensity, k is the wave vector and L_{eff} is the effective length. Full simulation of optical pulse propagation [86] is performed by using the experimentally measure nonlinear coefficients, and the corresponding transmitted spectrum are plotted using solid black lines in Fig. 3.10. As can be seen here, excellent agreement between theory and experiment is found, indicating that the third order nonlinear effect measured from z-scan is indeed from the instantaneous Kerr response, and the contribution from thermal effect can be neglected.

To summarize this section, we demonstrated giant Kerr nonlinear responses in MQW structures by the combination of the quantum size effect and the high free electron density of metal. The measured nonlinear Kerr susceptibility $|\chi^{(3)}|$ reaches as high as 2.06×10^{-15} m^2V^{-2}, showing

a 4 order-of-magnitude enhancement compared to the intrinsic value of bulk gold [52,75]. Spectral broadening measurements confirm that the 3rd order nonlinear effect is an instantaneous Kerr response. We expect that MQW structures can be easily combined with existing nano-photonic waveguides for integrated nonlinear optics, opening new opportunities for on-chip nonlinear optical applications with exceptionally high integration density. More extended applications based on the giant Kerr response will be discussed more in the next chapter.

Chapter 3, section 1, in part, has been submitted for publication of the material as it may appear in Light : Science & Applications (2018), Haoliang Qian, Shilong Li, Ching-Fu Chen, Su-Wen Hsu, Steven Edward Bopp, Qian Ma, Andrea R. Tao and Zhaowei Liu. The dissertation author was the primary investigator and author of this paper. Chapter 3, section 2, in part, is a reprint of the material as it appears in Nature Communication 7, 13153 (2016), Haoliang Qian, Yuzhe Xiao, Zhaowei Liu. The dissertation author was the primary investigator and author of this paper.

Chapter 4

Applications of plasmonic materials in quantum region

As we have discussed in the Chapter 2 and 3, the plasmonic materials in quantum region shows new features for both the linear and nonlinear properties. With the detailed exploration about the underlying physics in Chapter 2 and a few experimental demonstration in Chapter 3, here, we would like to talk more about the further application based on the quantum plasmonic materials. In this chapter, we will focus on more practical devices. In the first section, we would like to demonstrate that efficient light generation can happen in pure plasmonic materials by making two plasmonic nanostructures very close to each other, so that the electron wave in each nanostructure can be coupled, or in another word, the electron can tunnel through the gap between this two nanostructures. And by placing the metallic quantum well into the tunneling gap, resonant inelastic tunneling junction can be formed to boost up the internal quantum efficiency. In the second section, we would prove the exceptional performance of the optical pulse limiter by using the giant Kerr response from the metallic quantum well system, which extends the optical nonlinear devices, such as the sensor, to a severer condition previously thought impossible.

4.1 Light generation from Inelastic tunneling electrons

High speed light source is always desired for the optical communication, especially for the integrated optical inter-connect and optical information processing. Traditional plasmonic nanostructure would not meet the requirement for the light source due to the high loss from the metal. On the other hand, the plasmonic based devices possess the ultra-high speed response, which has already been used in many applications [9, 87]. Here, we would like to introduce the new way to generate the light from pure plasmonic nanostructures, which is based on the inelastic tunneling process. And by introducing the ultra-high plasmonic field into the inelastic tunneling process, efficient light emission can be realized. In order to do so, the plasmonic nanostructure need to be placed closer enough, such as 1 or 2 nm, so that the electrons can tunnel from one to another and overlap with the gap plasmon very well. By doing so, around 2% light generation has been demonstrated. Further enhancement of the light emission can be engineered by inserting the metallic quantum well into the gap between two plasmonic nanostructure. In this case, resonant inelastic tunneling can be formed, which could greatly boost up the emission efficiency.

Electrons can tunnel through a metal-insulator-metal (MIM) junction either elastically or inelastically. For elastic tunneling, electrons tunnel across the barrier layer without energy loss [88]. On the other hand, the inelastic tunneling process may create either phonons or photons as the electrons loose partial of their energy in the gap and transit to a lower energy state in the counter metal electrode. This process can be enhanced in the presence of surface plasmon polaritons (SPPs) around the MIM junction, as first discovered by Lambe and McCarthy in 1976 [89]. Later theoretical [90] and experimental [91–94] studies further augmented the appealing properties of MIM junction due to its ultra-small footprint and ultra-large modulation bandwidth. However, the major challenge for light generation from inelastic electron tunneling is its low external quantum efficiency (EQE), a production of internal quantum efficiency (IQE) and radiation efficiency (RE). Generally, the IQE describes the efficiency of the inelastic tunneling

event and can be increased by designing a plasmonic structure with a large local density of optical states (LDOS) [91,95,96], while the RE can be improved by introducing a high quality optical antenna [14,97]. Recently, light emission from electrically driven optical antennas made by amorphous (polycrystalline) plasmonic material has been demonstrated [98,99], with quantum efficiencies up to 10^{-4}. Compared with amorphous or polycrystalline plasmonic material, the single-crystalline material possesses the lower plasmonic loss [100] which can further enhance the performances of the inelastic tunnel junction. In this study, we use single-crystalline silver (Ag) nanocrystals to form the tunnel junctions with gap distances of 1.5 nm. Through the geometrical engineering of the junctions to optimize the LDOS and RE, the obtained far-field light emission efficiency reaches up to 2% at near infrared (NIR) frequencies, showing over two orders of magnitude improvement compared with previous reports [98,99].

The inelastic tunneling device is schematically illustrated in Fig. 4.1(a), where photons are emitted from an electronically biased junction formed by two Ag nanocrystals. Nanojunction assembly and orientation are carried out using a previously reported polymer mediated nanoparticle assembly process [101]. The gap distance in tunnel junction can be precisely controlled by the length of grafted polymers on the cuboid surfaces. The TEM image in Fig. 4.1(b) conforms that the gap of the tunnel junction is approximately 1.5 nm. High resolution TEM (HRTEM) in Fig. 4.1(c) confirms that the Ag structure is single-crystalline, which is critical to form high quality junction and optical antenna.

The total light emission is proportional to the IQE and RE [99]. The former is described by the Fermis golden rule which is related to the applied bias voltage, and the LDOS. The LDOS can be obtained by $\rho_p = \rho_0 \times (P_{tot}/P_0)$, where ρ_0 is the vacuum density of states (DOS), P_{tot} is the total dissipated power, and P_0 is the radiated power of a dipole of equal dipole moment in a vacuum environment. The RE is typically calculated by the ratio between radiative power and the total power. The plasmonic mode within the atomic level smoothed ultrasmall tunneling gap processes ultra-strong plasmonic field, causing the dramatically enhanced coupling strength

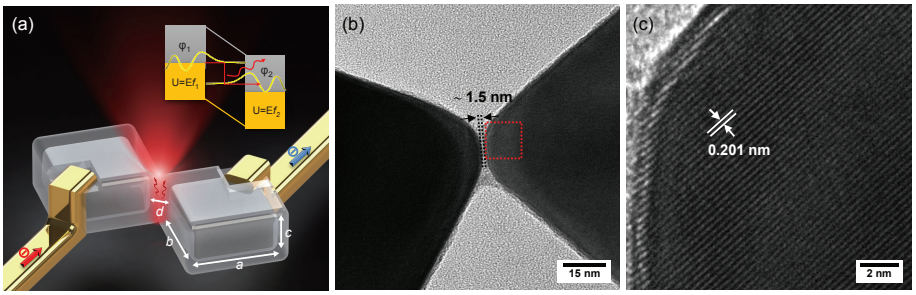

Figure 4.1: Light emission from an electrically driven atomic level engineered optical antenna. (a) Schematics of the tunnel junction formed by two edge-to-edge Ag single crystal cuboids capsulated by a layer of polymer. Here the grafted polymer (polyvinylpyrrolidone (PVP)) is acted as an insulating barrier due to the band gap of PVP larger than 4.7 eV [102]. The top inset shows that the photons are generated through inelastic electron tunneling. The device performance can be engineered by tuning the geometrical parameters of the tunnel junction including the gap size d, the size of the cuboids, a, b, c, and the curvature of Ag cuboid edges. (b) TEM image of the tunnel junction, where the gap is around 1.5 nm. (c) Single crystal lattice of the Ag facet near the tunnel junction (red dash square in (b)) taken by high-resolution TEM. The lattice distance is about 0.201 nm which corresponds to the Ag $\{200\}$ lattice spacing.

between the two electronic states (φ_1 and φ_2 marked in the inset of Fig. 4.1(a)), which could greatly increase the IQE. Through the engineering the geometry of the nano-junction with different heights (c) of the Ag square prisms and in-plane aspect ratio (b/a) of Ag nanobars, the overall efficiency can be tuned and optimized at a desired working frequency range.

Figure 4.2(a) shows the simulated LDOS and RE with different dipole polarizations in the center location of the gap, where one can see that x polarization dominates the LDOS and RE. Remarkably, the maximum LDOS and RE is 3.1×10^5 and 24.6% for the x-polarization, respectively. The plasmonic resonance field distribution shows that the plasmonic field is concentrated within the gap and overlaps with the junction very well, which greatly promotes the inelastic tunneling process due to the stronger electron-plasmon interaction [89]. Noted here that for 1.5 nm gap, it only gives very slight modification on the plasmonic resonance when considering either the nonlocal effect [103] or the quantum correlated model [37].

We started with electrical and optical characterization of a junction device formed by two Ag nanocubes with 70 nm in size. Using the applied voltage which corresponds to the maximum light emission, the emission spectrum of nanojunction (red circle in Fig. 4.2(b)) shows a clear

peak at 680 nm which agrees well with the simulation result (red solid curve in Fig. 4.2 (b)). Once the light emission power is obtained, the EQE (number-of-photon/number-of-electrons) of the Ag-cube tunnel junctions can be calculated. This gives a result of $(1.8 \pm 0.2) \times 10^{-3}$ at the peak location of the light emission power, showing one-order improvement compared with previous work using optical antenna.

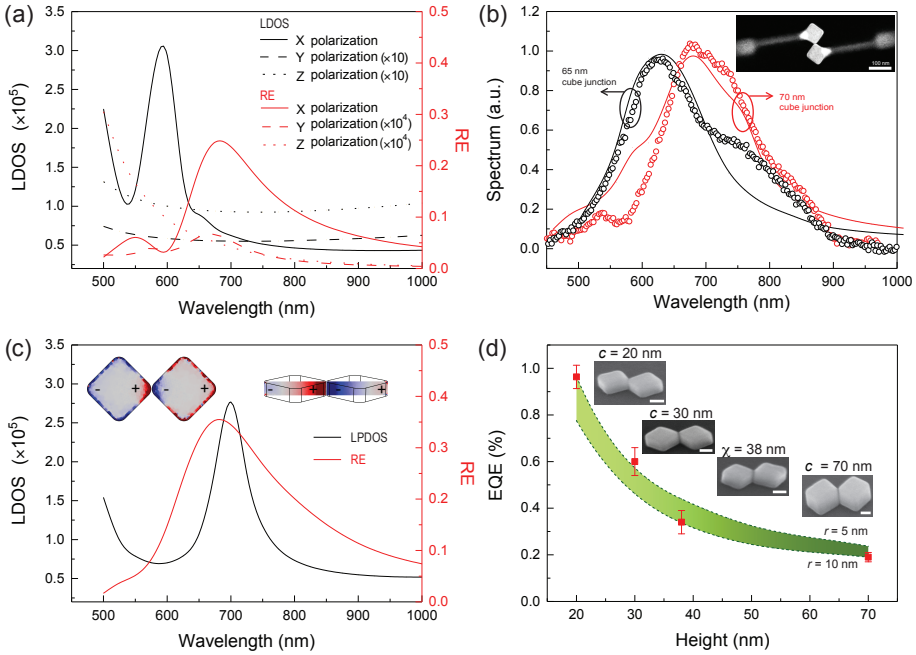

Figure 4.2: Investigation of the Ag square prism based tunnel junctions. (a) LDOS and RE of the Ag cubes (70 nm with edge curvature of 10 nm) with different dipole polarizations in the center location of the gap. (b) Emission spectrum with 3.2 V applied across the tunnel junctions. The black (65 nm) and red (70 nm) circles represent measurement data. The solid lines are simulation curves by averaging *x*-polarized dipoles at multiple locations inside the gap. Inset: Top-view SEM image of the tunnel junction after Pt electrode deposition. (c) The LDOS and RE of the Ag square prisms with height c = 20 nm. The top insets show the charge distribution at the peak wavelength of the LDOS (700 nm). (d) Experimental and simulated EQE of the tunnel junctions (a=b=70 nm, c=20 to 70 nm). The green area represents the simulation results with the edge curvature as 5 nm and 10 nm respectively. The red squares are the experimental results. The error bars represent the standard deviation from the multiple devices measurement. The side-view SEM images placed nearby shows the samples used for the experiment. The scale bar is 40 nm.

Before we further explore the details of the Ag nanocube junction, we would like to describe the measurement method here. The IV measurement is done with Agilent B1500

semiconductor device analyzer, together with light emission detection by PMT from Hamamatsu Photonics (H10720) and InGaAs amplified photodetector from Thorlabs (PDF10C). The spectrum is obtained with monochromator iHR550 from Horiba. All the electronic and optical components are integrated with probe stations with microscope objective of 20X (NA=0.45) and 50X (NA=0.8). The 20X objective is used for the electrical probes connection on the device and 50X objective is used for the optical signal detection. For the voltage dependent emission power measurement, the monochromator is set as 10 nm bandwidth and 10 nm increment step ensuring that the signal within [λ-5nm, λ+5nm] can be collected for each step. The total optical power emitted from the device can be obtained as follows:

$$P_{total} = \frac{1}{\eta_1} \sum \frac{P_{measurement}(\lambda)}{\eta_2(\lambda)} \tag{4.1}$$

where η_1 is the light collection efficiency of the microscope objective and η_2 is the detection efficiency of the system. The light collection efficiency (η_1) is estimated to be $\sim 28\%$, considering the NA=0.8 objective and the in-plane (XY plane) dipole radiation pattern. The wavelength dependent detection system efficiency $\eta_2(\lambda)$ is characterized by placing a tunable single wavelength laser source (laser source NA is smaller than the objective NA=0.8) with known power at the sample position and collecting the signal from the optical detector (shown in the Fig. 4.3(a-b)), which gives $\eta_2(\lambda)$=power obtain from detector / power input as shown in the Fig. 4.3(c). The monochromator placed at the image plane has the F-number of f/6.4, where the collection NA is much larger than the optical signal at the image plane considering the 50X NA=0.8 objective. Also the monochromator slit is much larger than the nanojunction size on the image plane. So there is no issue to couple all the light at the image plane into the monochromator. Note that majority of the objectives have the lower transmission efficiency at higher collection angle, so the $\eta_2(\lambda)$ characterized here using tunable single wavelength with limited NA is a little bit overestimated for the measurement system, which will give slightly underestimated total optical

power from the inelastic tunneling device.

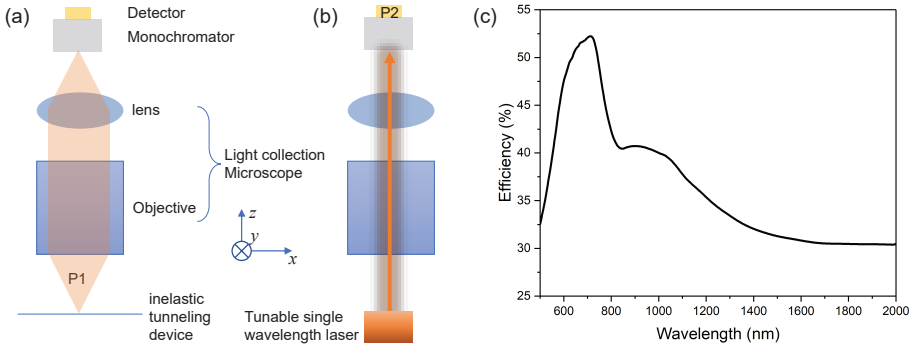

Figure 4.3: Measurement setup for the inelastic tunneling junctions. (a) Schematic drawing of the measurement setup. (b) Characterization of the measurement system efficiency. P1 represent the light collection efficiency (η_1) and P2 is the detection efficiency (η_2) of the system.The wavelength dependent detection system efficiency $\eta_2(\lambda)$ for the visible to near-infrared measurement range. The $\eta_2(\lambda)$ is calculated by power obtain from detector / input power.

One advantage of the metallic nanocrystal junction for light generation is the high tunability of the emission wavelength, which can be achieved by changing the size of nanocrystal. In order to further confirm such scalability, 65 nm cube tunnel junction is chosen and the corresponding emission spectrum measurement is shown as well in Fig. 4.2(b) (black circle). As expected, the emission spectrum shifts to a shorter wavelength (peak 625 nm). The obtained EQE of this tunneling device is $(1.9 \pm 0.2)10^{-3}$, similar to the case of 70 nm Ag-cube junction device.

As can be seen from the Fig. 4.2(a), the peak of the LDOS and RE are misaligned, which limit the light generation performance. The charge distribution of the nanocube junction at peak wavelength of the LDOS shows its high order nature which leads to the misalignment considering the dipole mode resonance of RE. Further improvement of the device performance can be achieved by aligning the peaks of LDOS mode with RE at the same emission wavelength, which is demonstrated by shrinking the height of the cube to square prism. Figure 4.2(c) shows the simulated LDOS and RE for the Ag square prism based tunnel junction with height c = 20 nm. The corresponding charge distribution at the peak wavelength of the LDOS was presented in the top

insert of Fig. 4.2(c), which confirms the dipole mode oscillation. In order to fabricate the square prism tunnel junction, we synthesized the square prism nanoparticle by polyol synthesis process and generated the square prism nanojunction in polystyrene matrix [104]. The experimental characterization of EQE in square prism nanojunctions shows that EQE is gradually improved by reducing the height of square prisms, which agrees well with numerical predictions (see Fig. 4.2(d)). This optimization process improves the EQE of the nanojunction device to about 1%.

Another strategy to enhance the EQE of the tunnel junction is to change the planar aspect ratio (b/a). With increasing b/a values, the LDOS gradually increased and both LDOS and RE peaks shifted to longer wavelength with lower plasmonic loss, leading to improved EQE compared to the case of nanocube junction with b/a = 1. The experimentally characterized EQE of nanobar junction with different b/a values (red square in Fig. 4.4) shows increased EQE with higher b/a value, which agrees well with the simulated prediction as shown in green colored area in Fig. 4.4. The b/a = 3.8 nanobar junction shows the EQE of $(1.10 \pm 0.07) \times 10^{-2}$ which is 5.5 times higher than the 70 nm nanocube junction. Noted that the deviation of the experimental results and simulated predictions may result from the varied radius of curvature at the edge of nanobar devices.

The EQE of tunnel junction can be further improved to $\sim 2\%$ (as black square in Fig. 4.4) by using the nanojunction with b/a = 4 and c = 20 nm nanobars, a combination of optimized height and the increasing b/a value of nanobar. In Fig. 4.5(a), it shows the measured light emission power detected at different voltages. The $(2.10 \pm 0.07) \times 10^{-2}$ EQE is calculated by using the maximum emission power (Fig. 4.5(b)) at applied voltage ~ 1.5 V. The voltage dependent light emission power is an interplay from the threshold voltage, inelastic tunneling current and the coupling between two electronic states φ_1 and φ_2. The emission spectrum shows the maximum light generation at ~ 1500 nm under the applied voltage of 1.5 V, which agrees well with the simulated prediction (solid line in Fig. 4.5(b)). Figure 4.5(c) shows that the emission is highly anisotropic and mainly dominated by x polarization as red circles, which agrees with the simulation result

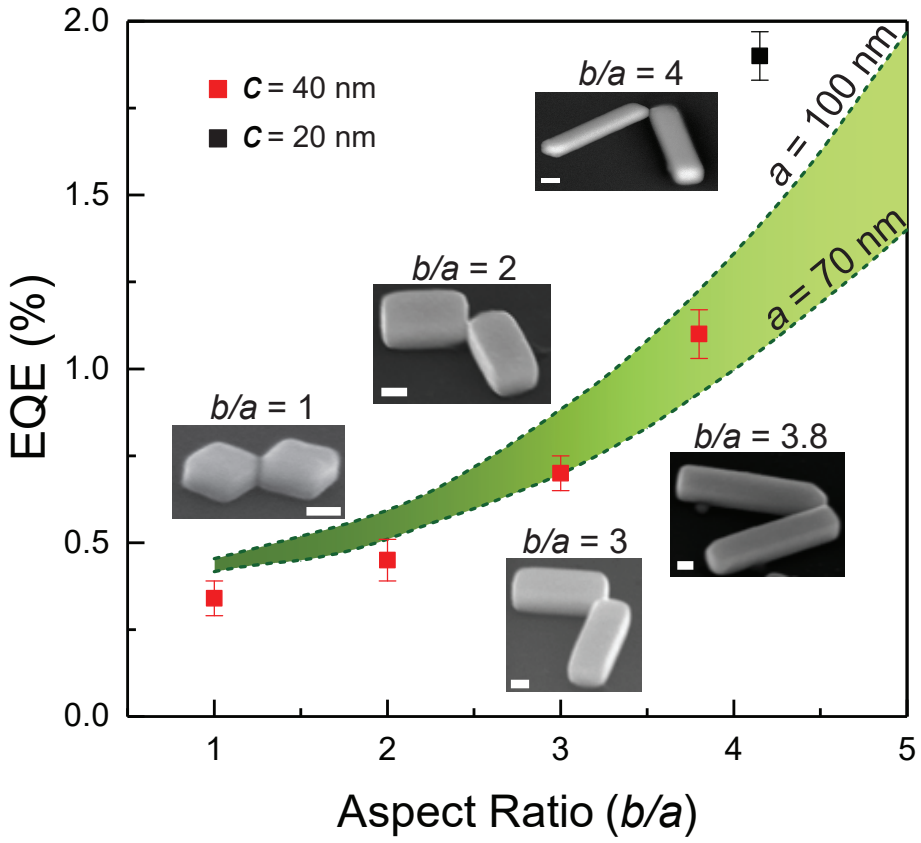

Figure 4.4: Numerical and experimental study of the Ag nanobar based tunnel junctions. Simulated and experimental EQE with respect to various b/a ratio. The green area bounded by the two curved dashed lines represents the simulation results with one planar width (a) of 70 nm and 100 nm respectively. The red and black squares are the experimental characterized result with c=40 and c=20 respectively. The error bars represent the standard deviation from the measurement result of multiple devices. The side-view SEM images placed nearby shows the samples used for the experiment. The scale bar is 40 nm.

(blue solid curve) very well. The *x*-polarized emission pattern further verifies the dipole mode emission from the Ag nanocrystal tunnel junctions.

To summarize what we had just described here, light generation through inelastic electron tunneling has been explored in the Ag tunnel junction structures with various geometries. With the assistance of the high RE formed by edge-to-edge assembled single crystalline Ag nanoantenna while maintaining the large LDOS in the ultra-small atomic level tunneling gap, we have dramatically increased the far-field light emission efficiency from spontaneous inelastic tunneling to 2%. In principle, the emission frequency of the MIM junction device can cover from

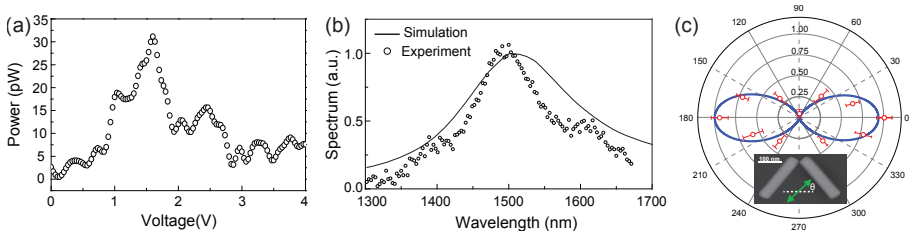

Figure 4.5: Ag nanobar based tunnel junction with optimized EQE. (a) Experimental characterization of the emission power at different voltages. (b) Emission spectrum measured with applied 1.5V. (c) Emission polarization result from both the simulation (blue line) and experimental measurement (red circle). The error bars represent the standard deviation from the measurement result of multiple devices. The simulation is done with a dipole placed in the center of the gap with the *x*, *y* and *z* polarizations and take the far-field radiation result. The angle corresponds to θ as marked in the top-view of the Ag nanobar junction with size of [280 65 20] nm. The white dash line represents the device direction and the green arrow for the direction of the detection polarizer.

UV all the way to mid-infrared, although the detailed material and junction configurations need to be designed accordingly. Implementing optical interconnections using tunnel junction based light emitting sources will make it possible to achieve extremely large bandwidth for drastically improved speed and quality of communications [105–107].

Further enhancement of external quantum efficiency may include reducing the gap distance between the nano-crystals in tunnel junction and improving the shape of nanocrystal with small curvature radius in the corner. As shown in Fig. 4.6, the theoretically predicted EQE of nanobar tunnel junction with c= 20 nm can be enhanced to 10% scale with emission peak in the near infrared region by using curvature radius of 2 nm at corner and the 1 nm gap. The other strategy to improve the performance includes low temperature operation which results from the higher figure-of-merit of the plasmonic material and improved thermal stability.

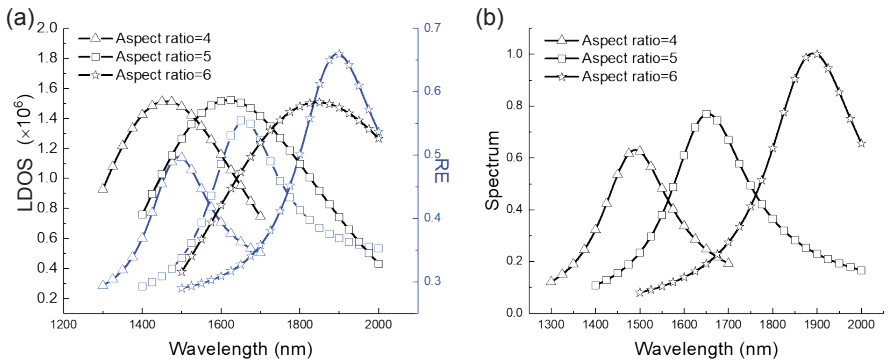

Figure 4.6: Simulation result of the nanobar junction with a gap of 1 nm and edge radius of 2 nm. (a) LDOS and RE for the nanobar junction with an aspect ratio of 4 (triangle), 5 (square) and 6 (star). The simulation is done by placing the dipole inside the gap and the angle between each nanobar is selected as 90 to form the junction. (b) Simulated emission spectrum based on the LDOS and RE. Considering the LDOS and RE for each aspect ratio (AR), the EQE can be 6.5% for the AR=4, 8% for AR=5 and 10.5% for the AR=6.

To add some more discussion about the thermal stability, which could be one of the major challenge for the practical application. The stability of the tunneling junction devices is mainly controlled by the insulating material between the nanojunction. Common breakdown strength for the insulating polymer, such as PVP and polystyrene, is around 0.5$\sim$1 V/nm with electrical lifetime about 10 seconds [108, 109]. These values were measured by few hundred nanometers to few micrometer thin films between two electrodes. According to the previous literature reports [110–113], the breakdown strength in a pair of nano-electrodes with small gap increases about 3$\sim$5 times with the electrode area decreasing to 10$\sim$100 nm^2 region. Because our edge-to-edge nanojunction area is below the 100 nm^2 with the junction gap about 1.5 nm, we expect the breakdown strength much higher than 1 V/nm, which causes stable operation of nanojunction at around 2$\sim$4 V for at least a few seconds. The I-V and light emission measurement of a single nanojunction only takes few seconds, which reduces the breakdown probability. We did notice that the breakdown of nanojunction occurs at applied voltage higher than 4.5 V. And we attribute the device failure to electrical breakdown and thermal damage. There are three strategies to elongate the device lifetime: (1) enhance the breakdown strength of device by lower temperature operation. (2) increase the thermal stability of device by replacing the PVP with

more durable material such as Al_2O_3. (3) further increase the light emission efficiency so that less energy will be dumped into heat, which would be a win-win situation.

Based on what we had discussed above, we got around 2% for the light generation from the plasmonic nanostructures by engineering the LDOS and RE. However, for these two parameters, there is not much room left for further enhancing the light emission with another order-of-magnitude. In the following part, we propose a strategy to overcome this challenging problem, through the inelastic electron-wave coupling by inserting the metallic quantum well into the plasmonic based tunneling junction as described above. The physical pictures are explained in the following Fig. 4.7. In Fig. 4.7(a), material system is schematically drawn that the metallic quantum well is placed inside the tunneling junction gap. Here the TiN is selected for the metallic quantum well due to the factor that TiN can be epitaxially grown with atomic smooth surface. In Fig. 4.7(b) and (c), the eigen-states and eigen-functions are calculated based on the quantum electrostatic model (Chapter 2) with 0 V and 2.4 V as the biased voltage for the MQW. As shown in Fig. 4.7(c), the injected electrons from the right side will have two possible channels. The first channel is plotted as the green dashed line, which represents the elastic tunneling current. The second channel is drawn with the red dashed line, which is the inelastic tunneling. For the elastic tunneling part, because the electron will need tunnel through two barriers, the tunneling probability is extremely small (as well as the current), while the inelastic tunneling event could happen when the energy difference between the energy level of the injected electrons and the Fermi energy for the left metal matches with the plasmonic gap resonance energy confined within the plasmonic nanostructures. In this case, the tunneling electrons through the first barrier can lose part of the energy to the plasmon and then tunnel through the second barrier with much higher probability, where this type of electron tunneling is called resonant tunneling.

The resonant tunneling junction has been widely used for the semiconductor quantum well system [114, 115] or molecule tunneling junctions [116]. Here, we would like to utilize the metallic quantum well to assist the inelastic tunneling process where the resonant tunneling

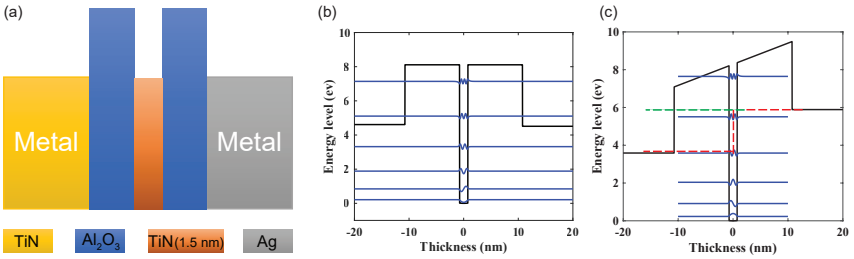

Figure 4.7: Working principle of the resonant inelastic tunneling junction. (a) Materials used for each layer of the resonant tunneling junction. (b) Eigen-function and eigen-states for the resonant tunneling junction at zero bias. (c) Eigen-function and eigen-states for the resonant tunneling junction at the bias of 2.4V.

condition is set for the inelastic tunneling event. The efficiency for light generation based on the inelastic resonant tunneling can be expressed as the following Eq. 4.2

$$\eta = \frac{\rho_{SP}}{\rho_{SP} + \rho_{elastic}} = \frac{\langle \varphi_1 | H_{SP} | \varphi_2 \rangle}{\langle \varphi_1 | H_{SP} | \varphi_1 \rangle + \rho_{elastic}} \tag{4.2}$$

In most cases, the elastic tunneling probability without aligning the Fermi level with any quantum states will be extremely small, and in this case, the final efficiency can be lift up closer to 100%. Since this enhancement is for the internal quantum efficiency, we would focus on the near-field surface plasmon generation so that high efficiency surface plasmon source can be realized within this type of inelastic tunneling junction. The designed structure is illustrated in Fig. 4.8(a) and the working device cross section is schematically shown in Fig. 4.8(b). Fig. 4.8(c) and (d) show the bright-field image of the fabricated device before the Ag nanowire transfer and dark-field image of the working area after placing the Ag nanowire, respectively. The Ag nanowire is coated with around 5 nm thick SiO_2, and the TEM image is presented in Fig. 4.8(e), showing the high quality nanowire and uniform oxide coating.

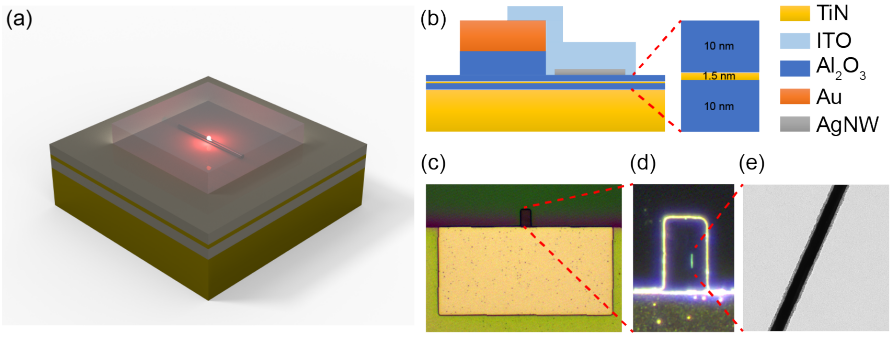

Figure 4.8: Resonant tunneling junction device. (a) Schematic illustration of the designed structures. (b) Cross-section drawing of the working device. (c) Bright-field optical image before the Ag nanowire transfer. (d) Dark-field optical image for the working area where the Ag nanowire can be clearly seen. (e) TEM image of the Ag nanowire used for the resonant tunneling junctions.

In order to determine the light generation performance of the fabricated resonant tunneling junctions, IV measurement and voltage dependent emission efficiency have been recorded, as shown in the Fig. 4.9(a) and (b), respectively. As one can see that, the maximum efficiency point corresponds to the applied voltage of 2.4V, which agree with the theoretical prediction in Fig. 4.7 (b) very well. The typical light emission result is recorded with the EMCCD, as shown in the inset of Fig. 4.9(b). The bright emission points at the end of the nanowire indicate the SPP generation and propagation along the nanowire and finally scattering out into far-field.

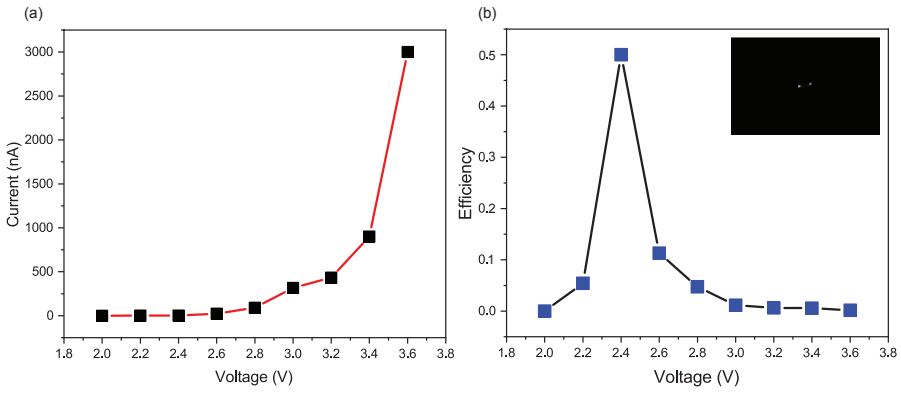

Figure 4.9: Experimental characterization of the resonant tunneling junction. (a) IV measurement. (b) Voltage-dependent light emission.

The result showing above gives the promising indication that the tunable, high-efficient

and compact SPP source can be realized in the resonant tunneling junction with the Ag nanowire. More detailed experimental studies and throughout theoretical calculation and explanation will be carried out in the future work. And it is expected that with the high-efficient optical antenna design on top of the resonant tunneling junctions, besides the Ag nanowire, more than 20% light emission generation into far field can be reached, which could enable more vital application in the area of integrated optics and optical communications.

4.2 Pulse limiter

An optical limiter provides a linear transmission/reflection below a certain threshold of intensity or power of incident light, while above the threshold it keeps the transmitted/reflected optical power below a specified value [117, 118]. The use of an appropriate limiter in front of an optical sensor, thus, not only protects the sensor but also extends its working range to a severer condition previously thought impossible. To this end, an active control of the limiting action would be quite attractive [117]. For example, a complex optical system consisting of detectors, processors, and actuators could restrict the incident light beam in a demand-oriented manner. However, the response time of any such active optical limiting device would be too long, which involves the time required by individual components to act in a sequential order and the time for communication between them. It is thus far slower than that of the commonly used fs laser sources. As a result, actively controlled optical systems are not suitable to limiting ultra-shot optical pulses. By contrast, passive optical limiters, which utilize materials possessing at least one optical nonlinear property, e.g., nonlinear refraction (self-focusing or defocusing) [117–119], nonlinear absorption (reverse saturable absorption (RSA) or multiple-photon absorption (MPA)) [118, 120–125], or nonlinear scattering (microbubbles or microplasmas) [126–128], could have a fast response time. Since most of these nonlinear processes are based on the optical Kerr effect, which can offer an ultrafast time response on the order of an electronic orbital period ($\sim 10^{-16}$

s) [53], Kerr-type nonlinear materials are crucial for passive optical limiters to controlling ultra-short optical pulses.

Kerr nonlinearity of a material is generally a third-order correction to its linear optical response and thus extremely weak [53]. As a consequence, Kerr-type passive optical limiting devices are ultimately made of macroscale solid or liquid media, in order to provide a long interaction length for accumulating sufficient nonlinearity, as sketched in Fig. 4.10(a),(b). There are a few weaknesses with these bulk optical limiters, such as the requirement of an additional intermediate focal plane [119], the difficulty in fabricating inhomogeneously distributed nonlinear media [122], and the possible distortion of wave-front and thus the degradation of beam quality. If possible, these drawbacks could be simply overcome by a reflective nanoscale optical limiter, such as the one shown in Fig. 4.10(c). Unfortunately, there is no report on materials or materials system that could provide a strong Kerr nonlinearity in nanoscale for the purpose of pulse limiting.

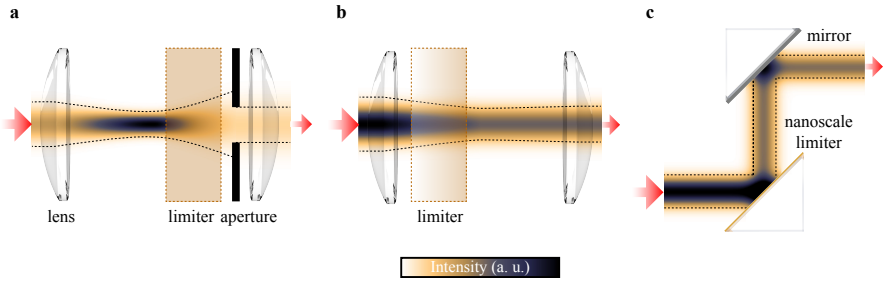

Figure 4.10: Comparison of the traditional bulk and the proposed nanoscale Kerr-type pulse limiters. (a),(b) Configurations (not to scale) widely used for optical limiting based on Kerr-induced self-defocusing (a) and Kerr-type nonlinear absorption (b), respectively. The former is achieved by inserting a bulk Kerr medium behind the focus plane to accelerate the divergence of incident Gaussian beam with a high intensity, so that only a fraction of the beam is allowed to pass through a preassigned aperture. The latter is done by putting a bulk Kerr medium before the focus plane to absorb the high-intensity portion of the incident beam. Note that an inhomogeneously distributed bulk Kerr medium, as shown in b, is desired to maximize the nonlinear absorption. (c) Concept of the nanoscale optical limiter (not to scale). The subwavelength-thin optical-limiting film can be integrated onto the surface of an existing optical component.

As we have demonstrated in the Chapter 3, giant Kerr nonlinearity has been obtained

in ultrathin Au films ($\sim$ 3nm thick), which is several orders larger than those of the traditional nonlinear materials. Such nontrivial strong Kerr nonlinearity is attributed to both a large electric dipole moment of the intersubband transition and a high free electron density in the metal, and can be well described by a QEM model. However, Au is not a durable material under ultra-strong optical field which hinder the extended application into the high-intensity ultra-shot pulse limiters.

Here in our study, we demonstrate a nanoscale Kerr-type optical limiter for fs pulses based on a durable MQW material system. It entirely consists of refractory materials [28], i.e., TiN and Al_2O_3 (as we had applied for the cMQW based SHG system), and thus ideal for high-intensity optical nonlinear applications. The typical transmission electron microscope (TEM) cross-section of the heterostructure is shown in Fig. 4.11(a),(b). The thickness of the TiN and Al_2O_3 layers is 2 nm and 2.4 nm, respectively. They were chosen to form the MQW by a unit of Al_2O_3/TiN/Al_2O_3 sandwich layer where the free electrons in such thin metallic well (TiN) are quantized between the neighboring dielectric barriers (Al_2O_3). As a result of the quantum sized effect, the electronic conduction band of bulk TiN is split into subbands. And, as will be shown below, large Kerr nonlinearities in the MQW arises owing to the resultant intersubband transitions. The calculated electronic band diagram of a single MQW unit, based on the QEM, is shown in Fig. 4.11(c), together with the dispersion of subbands. It is shown that the first six subbands are below the Fermi level and thus there would be a wealth of electronic transitions. As will be discussed later, they contribute to the pulse limiting effect via Kerr nonlinearity of the MQW intersubband system, as well as various multiple-photon transition (MPT) processes. Therefore, it is the plentiful electronic subbands to enable the unprecedented pulse limiting behavior of the nanoscale refractory thin films.

The nonlinear optical constant $n_{2(eff)}$ of TiN in the MQW was measured by the z-scan technique [74], and the result for a 45°-incidence *p*-polarized laser pulse with the intensity of 70 GW/cm^2 is summarized in Fig. 4.11(d). Resolved resonant peak, associated with the 1PT between subbands $|2\rangle$ and $|3\rangle$, as mentioned above, is observed in the dispersion curves

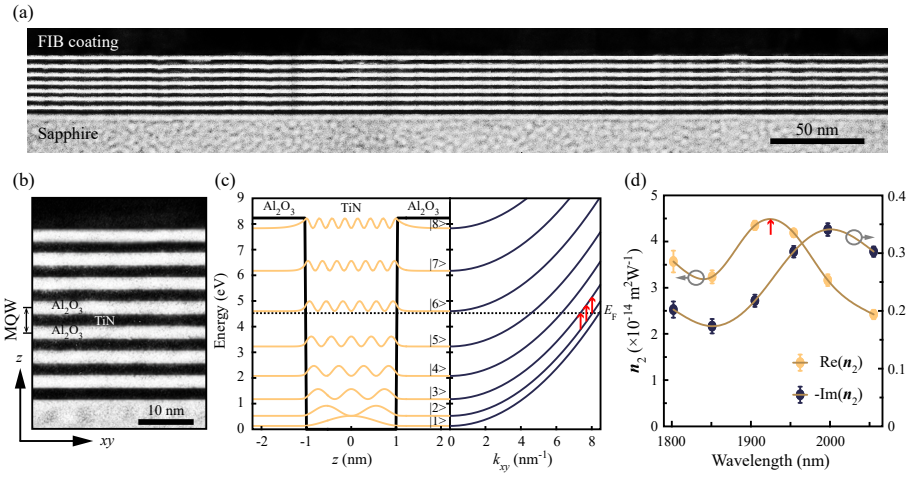

Figure 4.11: Realization of a nanoscale Kerr-type pulse limiter using MQW thin films. (a),(b) TEM cross-sections of MQW thin films made of refractory materials (TiN and Al_2O_3). The focused ion beam (FIB) coating forms a protective layer for the TEM cross-section preparation. (c) Conduction band diagram of a single MQW unit (left) and the corresponding electronic dispersion of subbands (right). The Fermi level E_F ($\sim$4.6 eV) is shown. The single red arrow indicates the single-photon transition between subbands $|2\rangle$ and $|3\rangle$. (d) Wavelength dependence of the nonlinear optical constant $n_{2(eff)}$) of TiN in the MQW. It was measured by the z-scan technique using 45°-incidence *p*-polarized laser pulses with the intensity of $\sim$70 GW/cm^2. The red arrow corresponds to the transition wavelength shown in (c)

of the $n_{2(eff)}$. It is the direct evidence of electron subbands resulting from the quantum size effect in the MQW. The amplitude of $n_{2(eff)}$ is several orders larger than those of the traditional nonlinear materials, and thus suitable for nonlinear-optics applications including the optical limiting. Moreover, the sign of real part of $n_{2(eff)}$, $\mathrm{Re}(n_{2(eff)})$, is positive while that of its imaginary part, $\mathrm{Im}(n_{2(eff)})$ is negative. As a result, the MQW would turn out to be a dielectric at high-intensity illumination. For this reason, the proposed optical limiter based on this MQW system works in a reflection mode, i.e., it allows a linear reflection for incident light with intensity below the threshold, while above the threshold it keeps the reflected optical power below a certain value. To the best of our knowledge, it is the first reflection-mode optical limiter, which gives a new degree of freedom for the optimal design of an optical limiting system.

Distinctly different from the conventional optical limiters, the nanoscale MQW thin film for a fs pulse limiting works in a reflection mode, as schematically shown in Fig. 4.13(a).

As a consequence, it can be integrated onto the surface of an existing optical component, and thus significantly simplifies the optical limiting configuration. Figure 4.13(b) depicts the intensity-dependent reflected power at 1997-nm wavelength for samples with a single unit and 7 units of MQWs, respectively. As can be clearly seen, there is a nearly linear reflection below a certain threshold of intensity, and above it the reflected power is below a certain value for the 7-unit MQWs sample in the intensity range. Compared to the 1-unit MQW sample, the sample covered by 7 units of MQW shows a distinct optical limiting performance, resulting from the Kerr-type nonlinearity engineering by metamaterials composed of dielectric and metallic multilayers [129], which has been indicated from different Kerr coefficient from the 7-unit MQW sample as shown in Fig. 4.12. This unprecedented tunability renders the nanoscale pulse limiters flexible and crucial in the design of compact optical and photonic systems.

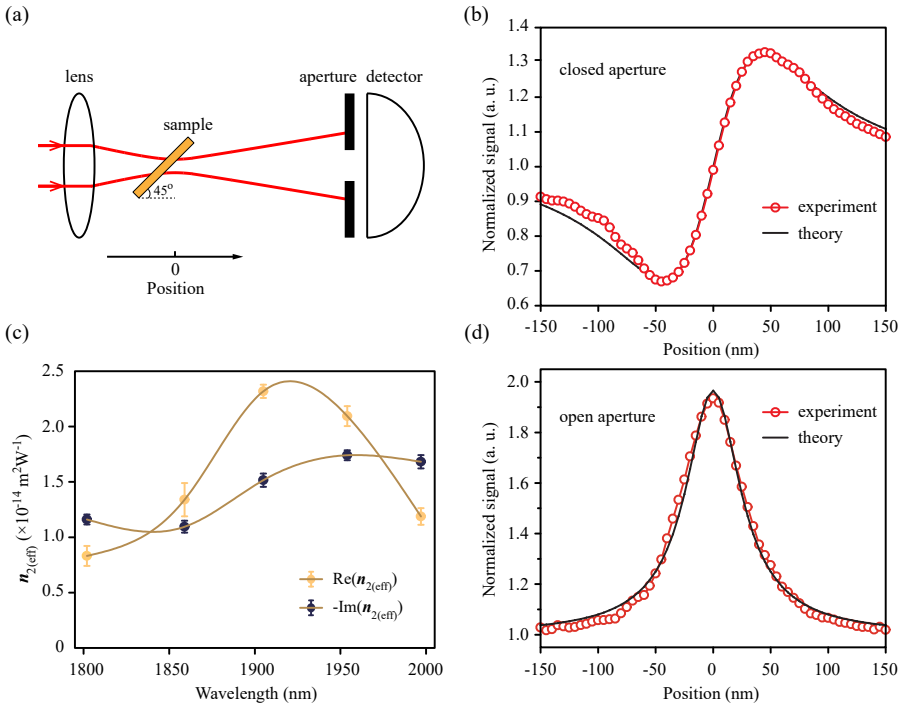

Figure 4.12: Z-scan measurement for the 7-unit of MQW pulse limiter sample. (a) Schematic of the z-scan setup. 45°-incidence p-polarized fs laser pulses are focused onto a MQW sample through a lens, while the MQW sample is moving along the optical axis near the focus of the lens. Two power detectors (only one of them schematically shown here) are used to collect the open (not shown here) and closed aperture z-scan signals. (b),(d) Closed (the upper panel) and open (the lower panel) aperture z-scan curves for the sample with 7 units of MQW under the pulse intensity of $\sim$ 70 GW/cm^2. The standard z-scan theory is applied to fit these experimental data, by which the nonlinear optical constant $n_{2(eff)}$ is extracted. (c) Wavelength dependence of the extracted $n_{2(eff)}$ of TiN in the 7-unit MQWs sample

Analogy to the conventional pulse limiter working in a transmission mode [119], several parameters for the proposed reflection-mode pulse limiter can be defined (see Fig. 4.13(b)). The first one is the linear reflectivity R_{lin} that is expected to be as higher as possible. The second parameter is the onset-of-limiting intensity I_{on}, which is defined as the incident intensity at which the reflectivity R drops off to $R_{lin}/2$. A tunable I_{on} is desired. The dynamic range DR is the third parameter and defined as $(I_{dam} - I_{on})/I_{on}$, where I_{dam} is the damage intensity of the MQW samples, which was determined experimentally shown in the Fig. 4.14. Larger DR it is, longer operating intensity range the pulse limiter supports. The last but not least one is

the reflectivity right before the damage, R_{dam}. For example, an optical limiting by the 7-unit MQW sample for 180-fs laser pulses at the center wavelength of 1997 nm is obtained with $R_{lin} \sim 32.3\%$, $I_{on} \sim 124$ GW/cm^2, DR $\sim 202\%$, and $R_{dam} \sim 6.8\%$. This unprecedented pulse limiting performance offered by the nanoscale MQW film is enabled by its large and ultrafast Kerr-type optical nonlinearities, and will be discussed in what follows.

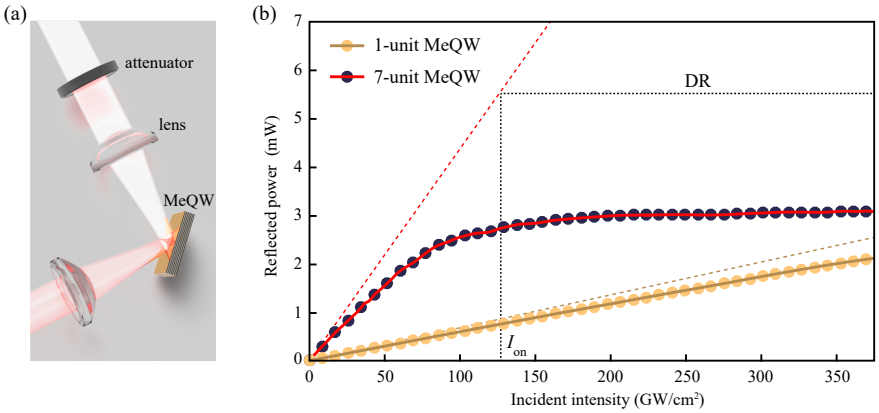

Figure 4.13: Performance of the reflection-mode nanoscale fs pulse limiter using MeQW thin films. (a) Experimental configuration (not to scale). (b) Intensity dependence of the measured reflected power for samples with a single unit and 7 units of MQWs at the wavelength of 1997 nm. The dashed lines show the correspond linear reflection curves. Relevant parameters are defined in the main text.

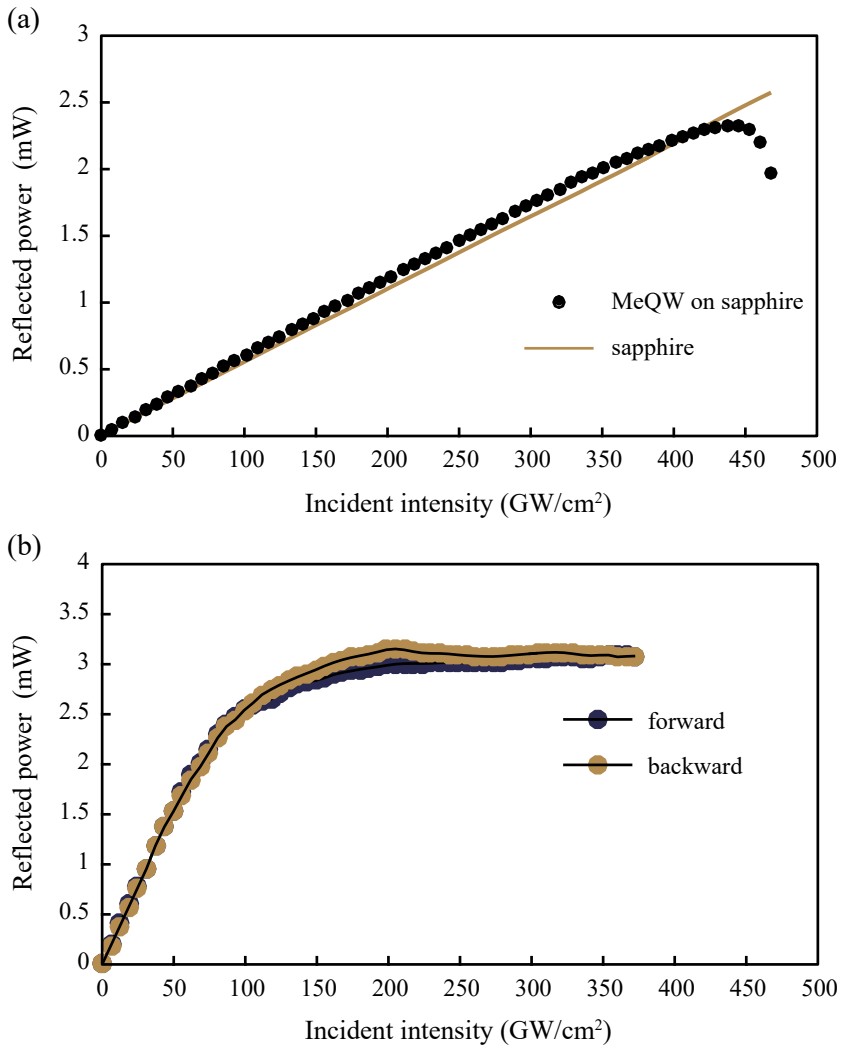

Figure 4.14: Determination of the damage intensity of MQWs. (a) Reflected power from samples with and without a single unit of MQW, respectively. Intensity at which the reflected power abruptly drops is defined as the damage intensity. (b) Below the damage intensity, the pulse limiting shows a good reproducibility

The $n_{2(eff)}$ obtained by the z-scan technique using a moderate-intensity laser pulse shows a large Kerr nonlinearity provided by the MQW. Generally, $n_{2(eff)}$ is dependent on the optical intensity, especially under a high-intensity illumination when the optical limiting is activated. Therefore, in order to further study the high-intensity nonlinearity, the reflectivity and transmittivity for 1997-nm laser pulses with various intensities up to 375 GW/cm^2 were measured, and then used to extract the intensity-dependent complex optical constant n_I $(n_I = n_0 + n_{2(I)}I)$

of TiN in the MQW for a given intensity I, and the results are summarized in Fig. 4.15(a). As can be seen, the $\mathrm{Re}(n_I)$ quickly jumps and saturates before entering the high-intensity range, and then drops, while the $\mathrm{Im}(n_I)$ monotonously decreases as the intensity increases, and keeps a small value at high intensity. Changes of 65% and 100%, respectively, in the real and imaginary parts of n_I are obtained, which again reveal the large nonlinearities in the MQW. In addition, the metal/dielectric transition is clearly visible in Fig. 4.15(a), as expected above.

The physics of the intensity-dependent Kerr nonlinearities supported by the MQW is discussed here. First of all, the strong Kerr response originates from the quantum sized effect. One can understand it by deriving the Kerr coefficient, which is proportional to $N_e(ez_{ij})^4/(\omega_{ij} - \omega - i\Gamma_{ij})^3$. Here, N_e, e and ω are the density of free electron, the electron charge, and the angular frequency of incident light, respectively. The intersubband dipole moment ez_{ij}, the electron transition frequency ω_{ij}, and the decay rate Γ_{ij} are associated with the involved optically active subbands. Due to both the large ez_{ij} and the high N_e, strong Kerr nonlinearities are obtained in the MQW. Secondly, these Kerr nonlinearities are also affected by the linear refractive index n_0 and thus can be tuned by means of metamaterials. Last but not least, several MPT processes contribute, concurrently, to these strong Kerr nonlinearities owing to the presence of the numerous subbands in the extremely deep metal QW. For example, the subbands $|2\rangle$ and $|3\rangle$ support a 1PT, while the concomitant two-photon absorption (TPA) occurs between the subbands $|5\rangle$ and $|6\rangle$, in the spectrum range considered (see Fig. 4.15(b)).

As mentioned above, the quantum size effect results in the strong Kerr coefficient of MQWs. As the consequence, the real part of n_I of the MQW samples quickly increases when the incident pulse intensity is increased. For the same reason, the imaginary part of n_I monotonously decreases. However, both the real and imaginary parts become saturated for sufficiently high intensity due to the saturation of the accompanied single-photon absorption (1PA) and two-photon absorption (TPA), which will be modeled according to the absorption saturation model.

The 1PA is associated with the intersubband transition from subbands $|2\rangle$ and $|3\rangle$, and it

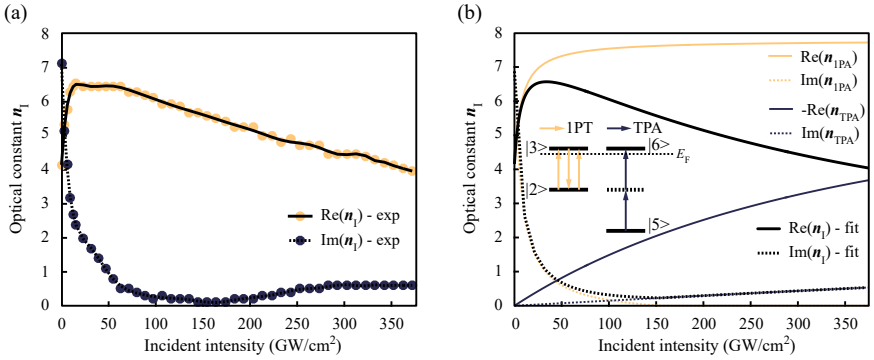

Figure 4.15: Physics of optical Kerr nonlinearities of the MQWs. (a),(b) Intensity-dependent refractive index n_I, respectively, extracted from the measured reflectivity and transmittivity (a), and fitted by the 1PA and TPA saturation models (b). Inset of (b) shows diagrams representing the 1PT (Kerr type, the left panel) and TPA (the right panel) processes, respectively. The sample used has 7 units of MeQW, and the data is taken at the wavelength of 1997 nm.

will be saturated above a certain intensity. The whole 1PA saturation process can be modeled [53, 130] by an intensity-dependent absorption coefficient $\alpha_I = \alpha_0/(1+I/I_{sat,1PA})$, where λ, α_0, and $I_{sat,1PA}$ are, respectively, the wavelength of incident light, the 1PA absorption coefficient constant, and the saturation intensity of 1PA. Similarly, the TPA from subbands $|5\rangle$ and $|6\rangle$ can also be modeled via the intensity-dependent absorption coefficient $\beta_I = \beta_0/(1+(I/I_{sat,TPA})^2)$ [130], where β_0 and $I_{sat,TPA}$ are the TPA absorption coefficient constant and saturation intensity, respectively. Therefore, the imaginary part of n_I in the entire intensity range is well fitted by the relation of $\mathrm{Im}(n_I) = \lambda(\alpha_I + \beta_I I)/(4\pi)$, as shown in Fig. 4.15(b).

Owing to both the 1PA and TPA, free electrons above the Fermi sea are continuously promoted. These promoted hot electrons above the Fermi sea can be described by the Drude model, and thus induce a negative change [131, 132] in the real part of n_I (i.e., $\mathrm{Re}(\Delta n_I) \propto -N_{hot}$, where N_{hot} is the density of the hot electrons), pulling down the real part of n_I at the high intensity. Combining the 1PA and TPA saturation models and the Drude model, the real part of n_I is well fitted.

To conclude this section, we have demonstrated a nanoscale reflection-mode fs pulse limiting thin film made of refractory materials. It is enabled by the large and ultrafast optical

Kerr nonlinearities of the embedded MQWs. These unprecedented intensity-dependent Kerr nonlinearities are attributed to the plentiful electron subbands in the MQW. Further efforts on the tunability of the nontrivial optical limiting, e.g., the working wavelength range and the working intensity range, could be made with the thin film consisting of different thickness of single MQW or coupled MQWs [54, 68]. By combining the MQWs (electron wavefunction engineering) and plasmonic metamaterials (photonic mode engineering), more degrees of freedom for the tunability could be involved, such as the incident angle and polarization. Further functionalization and integration of the Kerr-type nanoscale MQW thin film would enable vast applications for the on-chip integrated nonlinear optics .

Chapter 4, section 1, in part, is a reprint of the material as it appears in Nature Photonics 12, 485-488 (2018), Haoliang Qian, Su-Wen Hsu, Kargal Gurunatha, Conor T Riley, Jie Zhao, Dylan Lu, Andrea R Tao, Zhaowei Liu. The dissertation author was the primary investigator and author of this paper. Chapter 4, section 2, in part, is currently being prepared for submission for publication of the material, Haoliang Qian, Shilong Li, Yingmin Li, Ching-Fu Chen, Yeon-Ui Lee, Steven Edward Bopp, Wei Xiong, and Zhaowei Liu. The dissertation author was the primary investigator and author of this paper.

Chapter 5

Discussion, conclusion and outlook

Plasmonics has been well developed in the past few decades, which becomes a vital part for the optics field. In this thesis work, we introduce the quantum confinement into the plasmonics materials, such as the ultra-thin plasmonic layer or ultra-small tunneling gap between plasmonic nanostructures, to further extending the plasmonic field, exploring more for the underlying physics and making the plasmonic based devices more useful for the practical applications.

We first proposed a quantum electrostatic model to study the effect of the quantum confinement for both the linear and nonlinear optical properties. Then we demonstrated the giant nonlinearities, including the $\chi^{(2)}$ and $\chi^{(3)}$ by using the metallic quantum wells. After that, we focus on some of the real plasmonic devices, including realizing the high-efficiency light emission from pure plasmonic nanostructure with quantum sized tunneling gap, pushing the efficiency forward by introducing the metallic quantum well into the tunneling gap, and proving to have the exceptional pulse limiting performance by using the ultra-high Kerr response.

One step further, future research could focus on the coupling between the quantum well and quantum dot system, such as studying the lifetime engineering with the intersubband superradiance in the coupled quantum system. And for the direction of nonlinearity based on the

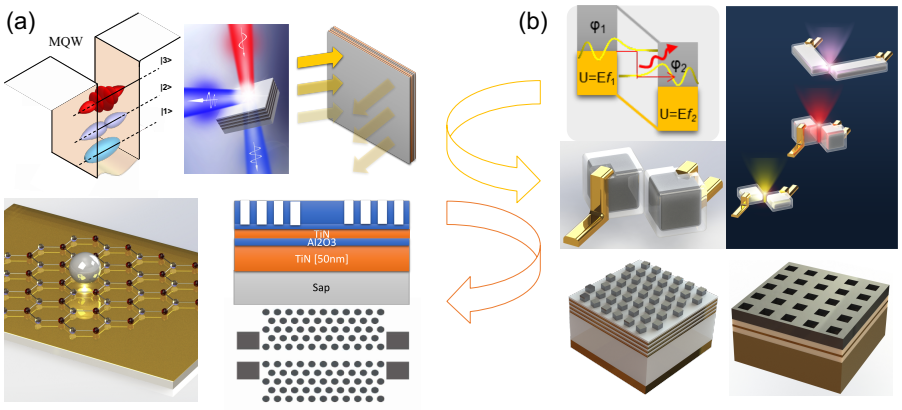

Figure 5.1: Efficient light-matter interaction from electron wave-function engineering (a) and the design of the plasmonic resonant cavities (b).

metallic quantum well, we could move forward to explore more practical devices, including the super-continuum generation by combining the photonic cavities with the metallic quantum wells. We summarize the all the studies and proposals in Fig. 5.1.

Eventually, our goal will gradually concentrate more on the light-matter interaction in quantum level, such as single molecule, or single quantum emitter with three-dimensional quantum confinment and single photon control and manipulation. More fruitful and exiting physics and application are expected for the future studying.

Bibliography

[1] Dmitri K. Gramotnev and Sergey I. Bozhevolnyi. Plasmonics beyond the diffraction limit. *Nature Photonics*, 4:83, 2010.

[2] Stefan Alexander Maier. *Plasmonics: fundamentals and applications*. Springer Science & Business Media, 2007.

[3] Ekmel Ozbay. Plasmonics: Merging photonics and electronics at nanoscale dimensions. *Science*, 311(5758):189–193, 2006.

[4] Jon A. Schuller, Edward S. Barnard, Wenshan Cai, Young Chul Jun, Justin S. White, and Mark L. Brongersma. Plasmonics for extreme light concentration and manipulation. *Nature Materials*, 9:193, 2010.

[5] Satoshi Kawata, Yasushi Inouye, and Prabhat Verma. Plasmonics for near-field nano-imaging and superlensing. *Nature Photonics*, 3:388, 2009.

[6] Xiaodong Yang, Jie Yao, Junsuk Rho, Xiaobo Yin, and Xiang Zhang. Experimental realization of three-dimensional indefinite cavities at the nanoscale with anomalous scaling laws. *Nature Photonics*, 6:450, 2012.

[7] Jeffrey N. Anker, W. Paige Hall, Olga Lyandres, Nilam C. Shah, Jing Zhao, and Richard P. Van Duyne. Biosensing with plasmonic nanosensors. *Nature Materials*, 7:442, 2008.

[8] Surbhi Lal, Stephan Link, and Naomi J. Halas. Nano-optics from sensing to waveguiding. *Nature Photonics*, 1:641, 2007.

[9] Masafumi Ayata, Yuriy Fedoryshyn, Wolfgang Heni, Benedikt Baeuerle, Arne Josten, Marco Zahner, Ueli Koch, Yannick Salamin, Claudia Hoessbacher, Christian Haffner, Delwin L. Elder, Larry R. Dalton, and Juerg Leuthold. High-speed plasmonic modulator in a single metal layer. *Science*, 358(6363):630–632, 2017.

[10] Gleb M. Akselrod, Christos Argyropoulos, Thang B. Hoang, Cristian Cirac, Chao Fang, Jiani Huang, David R. Smith, and Maiken H. Mikkelsen. Probing the mechanisms of large purcell enhancement in plasmonic nanoantennas. *Nature Photonics*, 8:835, 2014.

[11] Parinda Vasa, Wei Wang, Robert Pomraenke, Melanie Lammers, Margherita Maiuri, Cristian Manzoni, Giulio Cerullo, and Christoph Lienau. Real-time observation of ultrafast rabi oscillations between excitons and plasmons in metal nanostructures with j-aggregates. *Nature Photonics*, 7:128, 2013.

[12] Rohit Chikkaraddy, Bart de Nijs, Felix Benz, Steven J. Barrow, Oren A. Scherman, Edina Rosta, Angela Demetriadou, Peter Fox, Ortwin Hess, and Jeremy J. Baumberg. Single-molecule strong coupling at room temperature in plasmonic nanocavities. *Nature*, 535:127, 2016.

[13] En Cao, Weihua Lin, Mengtao Sun, Wenjie Liang, and Yuzhi Song. Exciton-plasmon coupling interactions: from principle to applications. *Nanophotonics*, 7(1):145, 2018.

[14] Lukas Novotny and Niek van Hulst. Antennas for light. *Nature Photonics*, 5:83–90, 2011.

[15] Jrmy Butet, Pierre-Franois Brevet, and Olivier J. F. Martin. Optical second harmonic generation in plasmonic nanostructures: From fundamental principles to advanced applications. *ACS Nano*, 9(11):10545–10562, 2015.

[16] Krishnan Thyagarajan, Simon Rivier, Andrea Lovera, and Olivier J. F. Martin. Enhanced second-harmonic generation from double resonant plasmonic antennae. *Optics Express*, 20(12):12860–12865, 2012.

[17] Seungchul Kim, Jonghan Jin, Young-Jin Kim, In-Yong Park, Yunseok Kim, and Seung-Woo Kim. High-harmonic generation by resonant plasmon field enhancement. *Nature*, 453:757, 2008.

[18] Pierre Berini and Israel De Leon. Surface plasmonpolariton amplifiers and lasers. *Nature Photonics*, 6:16, 2011.

[19] Martti Kauranen and Anatoly V. Zayats. Nonlinear plasmonics. *Nature Photonics*, 6:737, 2012.

[20] Kevin F. MacDonald, Zsolt L. Smson, Mark I. Stockman, and Nikolay I. Zheludev. Ultrafast active plasmonics. *Nature Photonics*, 3:55, 2008.

[21] P. DelHaye, A. Schliesser, O. Arcizet, T. Wilken, R. Holzwarth, and T. J. Kippenberg. Optical frequency comb generation from a monolithic microresonator. *Nature*, 450:1214, 2007.

[22] V. Brasch, M. Geiselmann, T. Herr, G. Lihachev, M. H. P. Pfeiffer, M. L. Gorodetsky, and T. J. Kippenberg. Photonic chipbased optical frequency comb using soliton cherenkov radiation. *Science*, 2015.

[23] P. DelHaye, O. Arcizet, A. Schliesser, R. Holzwarth, and T. J. Kippenberg. Full stabilization of a microresonator-based optical frequency comb. *Physical Review Letters*, 101(5):053903, 2008.

[24] Albrecht Bartels, Dirk Heinecke, and Scott A. Diddams. 10-ghz self-referenced optical frequency comb. *Science*, 326(5953):681–681, 2009.

[25] Xiao Tao Geng, Byung Jae Chun, Ji Hoon Seo, Kwanyong Seo, Hana Yoon, Dong-Eon Kim, Young-Jin Kim, and Seungchul Kim. Frequency comb transferred by surface plasmon resonance. *Nature Communications*, 7:10685, 2016.

[26] John M. Dudley, Gory Genty, and Stphane Coen. Supercontinuum generation in photonic crystal fiber. *Reviews of Modern Physics*, 78(4):1135–1184, 2006.

[27] A. V. Husakou and J. Herrmann. Supercontinuum generation of higher-order solitons by fission in photonic crystal fibers. *Physical Review Letters*, 87(20):203901, 2001.

[28] Urcan Guler, Alexandra Boltasseva, and Vladimir M. Shalaev. Refractory plasmonics. *Science*, 344(6181):263–264, 2014.

[29] P. Drude. Zur elektronentheorie der metalle. *Annalen der Physik*, 306(3):566–613, 1900.

[30] Mark I. Stockman. Nanoplasmonics: past, present, and glimpse into future. *Optics Express*, 19(22):22029–22106, 2011.

[31] M. S. Tame, K. R. McEnery, K. zdemir, J. Lee, S. A. Maier, and M. S. Kim. Quantum plasmonics. *Nature Physics*, 9:329, 2013.

[32] Jonathan A. Scholl, Ai Leen Koh, and Jennifer A. Dionne. Quantum plasmon resonances of individual metallic nanoparticles. *Nature*, 483:421, 2012.

[33] M. Khajavikhan, A. Simic, M. Katz, J. H. Lee, B. Slutsky, A. Mizrahi, V. Lomakin, and Y. Fainman. Thresholdless nanoscale coaxial lasers. *Nature*, 482:204, 2012.

[34] Kevin J. Savage, Matthew M. Hawkeye, Rubn Esteban, Andrei G. Borisov, Javier Aizpurua, and Jeremy J. Baumberg. Revealing the quantum regime in tunnelling plasmonics. *Nature*, 491:574, 2012.

[35] J. Dryzek and A. Czapla. Quantum size effect in optical spectra of thin metallic films. *Physical Review Letters*, 58(7):721–724, 1987.

[36] N. A. Mortensen, S. Raza, M. Wubs, T. Sndergaard, and S. I. Bozhevolnyi. A generalized non-local optical response theory for plasmonic nanostructures. *Nature Communications*, 5:3809, 2014.

[37] Ruben Esteban, Andrei G. Borisov, Peter Nordlander, and Javier Aizpurua. Bridging quantum and classical plasmonics with a quantum-corrected model. *Nature Communications*, 3:825, 2012.

[38] D. M. Wood and N. W. Ashcroft. Quantum size effects in the optical properties of small metallic particles. *Physical Review B*, 25(10):6255–6274, 1982.

[39] Dylan Lu, Jimmy J. Kan, Eric E. Fullerton, and Zhaowei Liu. Enhancing spontaneous emission rates of molecules using nanopatterned multilayer hyperbolic metamaterials. *Nature Nanotechnology*, 9:48, 2014.

[40] Slimane Laref, Jiangrong Cao, Abu Asaduzzaman, Keith Runge, Pierre Deymier, Richard W. Ziolkowski, Mamoru Miyawaki, and Krishna Muralidharan. Size-dependent permittivity and intrinsic optical anisotropy of nanometric gold thin films: a density functional theory study. *Optics Express*, 21(10):11827–11838, 2013.

[41] S. Schmitt-Rink, D. S. Chemla, and D. A. B. Miller. Linear and nonlinear optical properties of semiconductor quantum wells. *Advances in Physics*, 38(2):89–188, 1989.

[42] Nandini Trivedi and N. W. Ashcroft. Quantum size effects in transport properties of metallic films. *Physical Review B*, 38(17):12298–12309, 1988.

[43] J. J. Paggel, T. Miller, and T.-C. Chiang. Quantum-well states as fabry-prot modes in a thin-film electron interferometer. *Science*, 283(5408):1709–1711, 1999.

[44] J. J. Paggel, T. Miller, and T.-C. Chiang. Quantum-well states as fabry-prot modes in a thin-film electron interferometer. *Science*, 283(5408):1709–1711, 1999.

[45] W. B. Su, C. S. Chang, and T. Tsong Tien. Quantum size effect on ultra-thin metallic films. *Journal of Physics D: Applied Physics*, 43(1):013001, 2010.

[46] P. B. Johnson and R. W. Christy. Optical constants of the noble metals. *Physical Review B*, 6(12):4370–4379, 1972.

[47] Pochi Yeh, Amnon Yariv, and Chi-Shain Hong. Electromagnetic propagation in periodic stratified media. i. general theory*. *Journal of the Optical Society of America*, 67(4):423–438, 1977.

[48] N. D. Mermin. Lindhard dielectric function in the relaxation-time approximation. *Physical Review B*, 1(5):2362–2363, 1970.

[49] An analytic model for the optical properties of gold. *The Journal of Chemical Physics*, 125(16):164705, 2006.

[50] Richard P. Feynman. Quantum mechanical computers. *Foundations of Physics*, 16(6):507–531, 1986.

[51] A. V. Lugovskoy and I. Bray. Electron-electron scattering rate in thin metal films. *Physical Review B*, 65(4):045405, 2001.

[52] Robert W. Boyd, Zhimin Shi, and Israel De Leon. The third-order nonlinear optical susceptibility of gold. *Optics Communications*, 326(Supplement C):74–79, 2014.

[53] Robert W. Boyd. *Nonlinear Optics, Third Edition*. Academic Press, 2008.

[54] E. Rosencher, A. Fiore, B. Vinter, V. Berger, Ph. Bois, and J. Nagle. Quantum engineering of optical nonlinearities. *Science*, 271(5246):168–173, 1996.

[55] M. M. Fejer, S. J. B. Yoo, R. L. Byer, A. Harwit, and J. S. Harris. Observation of extremely large quadratic susceptibility at 9.6-10.8 m in electric-field-biased algaas quantum wells. *Physical Review Letters*, 62(9):1041–1044, 1989.

[56] Mordechai Segev, Ilan Grav, and Amnon Yariv. Demonstration of the optical kerr effect at 10.6 m via intersubband nonlinearities in a multiquantum well structure. *Applied Physics Letters*, 61(20):2403–2405, 1992.

[57] R. Paiella. *Intersubband Transitions In Quantum Structures*. McGraw-Hill Education, 2010.

[58] E.R. Weber, R.K. Willardson, H.C. Liu, and F. Capasso. *Intersubband Transitions in Quantum Wells: Physics and Device Applications*. Elsevier Science, 1999.

[59] P. R. West, S. Ishii, G. V. Naik, N. K. Emani, V. M. Shalaev, and A. Boltasseva. Searching for better plasmonic materials. *Laser & Photonics Reviews*, 4(6):795–808, 2010.

[60] Urcan Guler, Vladimir M. Shalaev, and Alexandra Boltasseva. Nanoparticle plasmonics: going practical with transition metal nitrides. *Materials Today*, 18(4):227–237, 2015.

[61] Gururaj V. Naik, Jongbum Kim, and Alexandra Boltasseva. Oxides and nitrides as alternative plasmonic materials in the optical range [invited]. *Optical Materials Express*, 1(6):1090–1099, 2011.

[62] Panos Patsalas, Nikolaos Kalfagiannis, and Spyros Kassavetis. Optical properties and plasmonic performance of titanium nitride. *Materials*, 8(6):3128, 2015.

[63] Gururaj V. Naik, Bivas Saha, Jing Liu, Sammy M. Saber, Eric A. Stach, Joseph M. K. Irudayaraj, Timothy D. Sands, Vladimir M. Shalaev, and Alexandra Boltasseva. Epitaxial superlattices with titanium nitride as a plasmonic component for optical hyperbolic metamaterials. *Proceedings of the National Academy of Sciences of the United States of America*, 111(21):7546–7551, 2014.

[64] Alexander Krasnok, Mykhailo Tymchenko, and Andrea Al. Nonlinear metasurfaces: a paradigm shift in nonlinear optics. *Materials Today*, 21(1):8–21, 2018.

[65] Guixin Li, Shuang Zhang, and Thomas Zentgraf. Nonlinear photonic metasurfaces. *Nature Reviews Materials*, 2:17010, 2017.

[66] Carlo Sirtori, Federico Capasso, Deborah L. Sivco, S. N. G. Chu, and Alfred Y. Cho. Observation of large second order susceptibility via intersubband transitions at 10 m in asymmetric coupled alinas/gainas quantum wells. *Applied Physics Letters*, 59(18):2302–2304, 1991.

[67] Fu Xiang Wang, Francisco J. Rodrguez, Willem M. Albers, Risto Ahorinta, J. E. Sipe, and Martti Kauranen. Surface and bulk contributions to the second-order nonlinear optical response of a gold film. *Physical Review B*, 80(23):233402, 2009.

[68] Jongwon Lee, Mykhailo Tymchenko, Christos Argyropoulos, Pai-Yen Chen, Feng Lu, Frederic Demmerle, Gerhard Boehm, Markus-Christian Amann, Andrea Al, and Mikhail A. Belkin. Giant nonlinear response from plasmonic metasurfaces coupled to intersubband transitions. *Nature*, 511:65, 2014.

[69] Andrej Grubisic, Emilie Ringe, Claire M. Cobley, Younan Xia, Laurence D. Marks, Richard P. Van Duyne, and David J. Nesbitt. Plasmonic near-electric field enhancement effects in ultrafast photoelectron emission: Correlated spatial and laser polarization microscopy studies of individual ag nanocubes. *Nano Letters*, 12(9):4823–4829, 2012.

[70] Michele Celebrano, Xiaofei Wu, Milena Baselli, Swen Gromann, Paolo Biagioni, Andrea Locatelli, Costantino De Angelis, Giulio Cerullo, Roberto Osellame, Bert Hecht, Lamberto Du, Franco Ciccacci, and Marco Finazzi. Mode matching in multiresonant plasmonic nanoantennas for enhanced second harmonic generation. *Nature Nanotechnology*, 10(5):412–417, 2015.

[71] Reza Salem, Mark A. Foster, Amy C. Turner, David F. Geraghty, Michal Lipson, and Alexander L. Gaeta. Signal regeneration using low-power four-wave mixing on silicon chip. *Nature Photonics*, 2:35, 2007.

[72] T. Gu, N. Petrone, J. F. McMillan, A. van der Zande, M. Yu, G. Q. Lo, D. L. Kwong, J. Hone, and C. W. Wong. Regenerative oscillation and four-wave mixing in graphene optoelectronics. *Nature Photonics*, 6:554, 2012.

[73] Joerg Pfeifle, Victor Brasch, Matthias Lauermann, Yimin Yu, Daniel Wegner, Tobias Herr, Klaus Hartinger, Philipp Schindler, Jingshi Li, David Hillerkuss, Rene Schmogrow, Claudius Weimann, Ronald Holzwarth, Wolfgang Freude, Juerg Leuthold, Tobias J. Kippenberg, and Christian Koos. Coherent terabit communications with microresonator kerr frequency combs. *Nature Photonics*, 8:375, 2014.

[74] M. Sheik-Bahae, A. A. Said, T. Wei, D. J. Hagan, and E. W. Van Stryland. Sensitive measurement of optical nonlinearities using a single beam. *IEEE Journal of Quantum Electronics*, 26(4):760–769, 1990.

[75] Jan Renger, Romain Quidant, Niek van Hulst, and Lukas Novotny. Surface-enhanced nonlinear four-wave mixing. *Physical Review Letters*, 104(4):046803, 2010.

[76] D. C. Marinica, A. K. Kazansky, P. Nordlander, J. Aizpurua, and A. G. Borisov. Quantum plasmonics: Nonlinear effects in the field enhancement of a plasmonic nanoparticle dimer. *Nano Letters*, 12(3):1333–1339, 2012.

[77] M.G. Papadopoulos, A.J. Sadlej, and J. Leszczynski. *Non-Linear Optical Properties of Matter: From molecules to condensed phases*. Springer Netherlands, 2007.

[78] Nir Rotenberg, A. D. Bristow, Markus Pfeiffer, Markus Betz, and H. M. van Driel. Nonlinear absorption in au films: Role of thermal effects. *Physical Review B*, 75(15):155426, 2007.

[79] Oleg Lysenko, Morten Bache, and Andrei Lavrinenko. Third-order susceptibility of gold for ultrathin layers. *Optics Letters*, 41(2):317–320, 2016.

[80] R. de Nalda, R. del Coso, J. Requejo-Isidro, J. Olivares, A. Suarez-Garcia, J. Solis, and C. N. Afonso. Limits to the determination of the nonlinear refractive index by the z-scan method. *Journal of the Optical Society of America B*, 19(2):289–296, 2002.

[81] z-scan measurement of the nonlinear absorption of a thin gold film. *Journal of Applied Physics*, 86(11):6200–6205, 1999.

[82] Pei Wang, Yonghua Lu, Li Tang, Jiangying Zhang, Hai Ming, Jiangping Xie, Fu-Han Ho, Hsun-Hao Chang, Hsia-Yu Lin, and Din-Ping Tsai. Surface-enhanced optical nonlinearity of a gold film. *Optics Communications*, 229(1):425–429, 2004.

[83] Matteo Conforti and Giuseppe Della Valle. Derivation of third-order nonlinear susceptibility of thin metal films as a delayed optical response. *Physical Review B*, 85(24):245423, 2012.

[84] Yannick Guillet, Majid Rashidi-Huyeh, and Bruno Palpant. Influence of laser pulse characteristics on the hot electron contribution to the third-order nonlinear optical response of gold nanoparticles. *Physical Review B*, 79(4):045410, 2009.

[85] C. K. Sun, F. Valle, L. H. Acioli, E. P. Ippen, and J. G. Fujimoto. Femtosecond-tunable measurement of electron thermalization in gold. *Physical Review B*, 50(20):15337–15348, 1994.

[86] G. Agrawal. *Nonlinear Fiber Optics*. Elsevier Science, 2012.

[87] C. Haffner, W. Heni, Y. Fedoryshyn, J. Niegemann, A. Melikyan, D. L. Elder, B. Baeuerle, Y. Salamin, A. Josten, U. Koch, C. Hoessbacher, F. Ducry, L. Juchli, A. Emboras, D. Hillerkuss, M. Kohl, L. R. Dalton, C. Hafner, and J. Leuthold. All-plasmonic machzehnder modulator enabling optical high-speed communication at the microscale. *Nature Photonics*, 9:525, 2015.

[88] Juan C. Ranurez, M. J. Deen, and Chih-Hung Chen. A review of gate tunneling current in mos devices. *Microelectronics Reliability*, 46(12):1939–1956, 2006.

[89] John Lambe and S. L. McCarthy. Light emission from inelastic electron tunneling. *Physical Review Letters*, 37(14):923–925, 1976.

[90] L. C. Davis. Theory of surface-plasmon excitation in metal-insulator-metal tunnel junctions. *Physical Review B*, 16(6):2482–2490, 1977.

[91] S. L. McCarthy and John Lambe. Enhancement of light emission from metalinsulatormetal tunnel junctions. *Applied Physics Letters*, 30(8):427–429, 1977.

[92] J. Kirtley, T. N. Theis, and J. C. Tsang. Light-emission from tunnel-junctions on gratings. *Physical Review B*, 24(10):5650–5663, 1981.

[93] Richard Berndt, James K. Gimzewski, and Peter Johansson. Inelastic tunneling excitation of tip-induced plasmon modes on noble-metal surfaces. *Physical Review Letters*, 67(27):3796–3799, 1991.

[94] P. D. Sparks, T. Sjodin, B. W. Reed, and J. Stege. Light-emission from the slow mode of tunnel-junctions on short-period diffraction gratings. *Physical Review Letters*, 68(17):2668–2671, 1992.

[95] Watanabe Junichi, Uehara Yoichi, Murota Junichi, and Ushioda Sukekatsu. Light emission from si-metal-oxide-semiconductor tunnel junctions. *Japanese Journal of Applied Physics*, 32(1R):99, 1993.

[96] D. P. Siu, R. K. Jain, and T. K. Gustafson. Stimulated electron tunneling in metalbarriermetal structures due to surface plasmons. *Applied Physics Letters*, 28(7):407–410, 1976.

[97] Palash Bharadwaj, Bradley Deutsch, and Lukas Novotny. Optical antennas. *Advances in Optics and Photonics*, 1(3):438–483, 2009.

[98] Johannes Kern, Ren Kullock, Jord Prangsma, Monika Emmerling, Martin Kamp, and Bert Hecht. Electrically driven optical antennas. *Nature Photonics*, 9:582, 2015.

[99] M. Parzefall, P. Bharadwaj, A. Jain, T. Taniguchi, K. Watanabe, and L. Novotny. Antenna-coupled photon emission from hexagonal boron nitride tunnel junctions. *Nature Nanotechnology*, 10:1058–1063, 2015.

[100] Sriharsha V. Jayanti, Jong Hyuk Park, Alexandr Dejneka, Dagmar Chvostova, Kevin M. McPeak, Xiaoshu Chen, Sang-Hyun Oh, and David J. Norris. Low-temperature enhancement of plasmonic performance in silver films. *Optical Materials Express*, 5(5):1147–1155, 2015.

[101] Bo Gao, Gaurav Arya, and Andrea R. Tao. Self-orienting nanocubes for the assembly of plasmonic nanojunctions. *Nature Nanotechnology*, 7(7):433–437, 2012.

[102] A Rawat, HK Mahavar, S Chauhan, A Tanwar, and PJ Singh. Optical band gap of polyvinylpyrrolidone/polyacrilamide blend thin films. *Indian J. Pure Appl. Phys.*, 50(2):100–104, 2012.

[103] F. Javier Garca de Abajo. Nonlocal effects in the plasmons of strongly interacting nanoparticles, dimers, and waveguides. *The Journal of Physical Chemistry C*, 112(46):17983–17987, 2008.

[104] Su-Wen Hsu and Andrea R. Tao. Halide-directed synthesis of square prismatic ag nanocrystals by the polyol method. *Chemistry of Materials*, 30(14):4617–4623, 2018.

[105] E. Fred Schubert and Jong Kyu Kim. Solid-state light sources getting smart. *Science*, 308(5726):1274–1278, 2005.

[106] Wei Du, Tao Wang, Hong-Son Chu, and Christian A. Nijhuis. Highly efficient on-chip direct electronicplasmonic transducers. *Nature Photonics*, 11(10):623–627, 2017.

[107] Yurui Fang and Mengtao Sun. Nanoplasmonic waveguides: towards applications in integrated nanophotonic circuits. *Light: Science & Applications*, 4:e294, 2015.

[108] V. A. Zakrevskii and N. T. Sudar. Electrical breakdown of thin polymer films. *Physics of the Solid State*, 47(5):961–967, 2005.

[109] M. Ieda. Dielectric-breakdown process of polymers. *Ieee Transactions on Electrical Insulation*, 15(3):206–224, 1980.

[110] S. Diaham, S. Zelmat, M. L. Locatelli, S. Dinculescu, M. Decup, and T. Lebey. Dielectric breakdown of polyimide films: Area, thickness and temperature dependence. *IEEE Transactions on Dielectrics and Electrical Insulation*, 17(1):18–27, 2010.

[111] Cdric Sire, Serge Blonkowski, Michael J. Gordon, and Thierry Baron. Statistics of electrical breakdown field in hfo2 and sio2 films from millimeter to nanometer length scales. *Applied Physics Letters*, 91(24):242905, 2007.

[112] M. L. Green, E. P. Gusev, R. Degraeve, and E. L. Garfunkel. Ultrathin (¡4 nm) sio2 and sion gate dielectric layers for silicon microelectronics: Understanding the processing, structure, and physical and electrical limits. *Journal of Applied Physics*, 90(5):2057–2121, 2001.

[113] K. Kato, X. Han, and H. Okubo. Insulation optimization by electrode contour modification based on breakdown area/volume effects. *IEEE Transactions on Dielectrics and Electrical Insulation*, 8(2):162–167, 2001.

[114] K. Ismail, B. S. Meyerson, and P. J. Wang. Electron resonant tunneling in si/sige double barrier diodes. *Applied Physics Letters*, 59(8):973–975, 1991.

[115] Selman Hershfield, John H. Davies, and John W. Wilkins. Probing the kondo resonance by resonant tunneling through an anderson impurity. *Physical Review Letters*, 67(26):3720–3723, 1991.

[116] Michael Galperin, Abraham Nitzan, and Mark A. Ratner. Resonant inelastic tunneling in molecular junctions. *Physical Review B*, 73(4):045314, 2006.

[117] Lee W. Tutt and Thomas F. Boggess. A review of optical limiting mechanisms and devices using organics, fullerenes, semiconductors and other materials. *Progress in Quantum Electronics*, 17(4):299–338, 1993.

[118] Gui-Jiang Zhou and Wai-Yeung Wong. Organometallic acetylides of ptii, aui and hgii as new generation optical power limiting materials. *Chemical Society Reviews*, 40(5):2541–2566, 2011.

[119] A. Nevejina-Sturhan, O. Werhahn, and U. Siegner. Low-threshold high-dynamic-range optical limiter for ultra-short laser pulses. *Applied Physics B*, 74(6):553–557, 2002.

[120] Shuzo Hirata, Kenro Totani, Takashi Yamashita, Chihaya Adachi, and Martin Vacha. Large reverse saturable absorption under weak continuous incoherent light. *Nature Materials*, 13:938, 2014.

[121] Geok-Kieng Lim, Zhi-Li Chen, Jenny Clark, Roland G. S. Goh, Wee-Hao Ng, Hong-Wee Tan, Richard H. Friend, Peter K. H. Ho, and Lay-Lay Chua. Giant broadband nonlinear optical absorption response in dispersed graphene single sheets. *Nature Photonics*, 5:554, 2011.

[122] J. W. Perry, K. Mansour, I.-Y. S. Lee, X.-L. Wu, P. V. Bedworth, C.-T. Chen, D. Ng, S. R. Marder, P. Miles, T. Wada, M. Tian, and H. Sasabe. Organic optical limiter with a strong nonlinear absorptive response. *Science*, 273(5281):1533–1536, 1996.

[123] Lee W. Tutt and Alan Kost. Optical limiting performance of c60 and c70 solutions. *Nature*, 356:225, 1992.

[124] Boshan Zhao, Baobao Cao, Weilie Zhou, Dan Li, and Wei Zhao. Nonlinear optical transmission of nanographene and its composites. *The Journal of Physical Chemistry C*, 114(29):12517–12523, 2010.

[125] Quanshui Li, Chunling Liu, Zhengang Liu, and Qihuang Gong. Broadband optical limiting and two-photon absorption properties of colloidal gaas nanocrystals. *Optics Express*, 13(6):1833–1838, 2005.

[126] Kamjou Mansour, M. J. Soileau, and E. W. Van Stryland. Nonlinear optical properties of carbon-black suspensions (ink). *Journal of the Optical Society of America B*, 9(7):1100–1109, 1992.

[127] Karen M. Nashold and Diane Powell Walter. Investigations of optical limiting mechanisms in carbon particle suspensions and fullerene solutions. *Journal of the Optical Society of America B*, 12(7):1228–1237, 1995.

[128] Laurent Vivien, Didier Riehl, Jean-Franois Delouis, Jacques A. Delaire, Franois Hache, and Eric Anglaret. Picosecond and nanosecond polychromatic pumpprobe studies of bubble growth in carbon-nanotube suspensions. *Journal of the Optical Society of America B*, 19(2):208–214, 2002.

[129] Andres D. Neira, Nicolas Olivier, Mazhar E. Nasir, Wayne Dickson, Gregory A. Wurtz, and Anatoly V. Zayats. Eliminating material constraints for nonlinearity with plasmonic metamaterials. *Nature Communications*, 6:7757, 2015.

[130] Guang S. He, Qingdong Zheng, Alexander Baev, and Paras N. Prasad. Saturation of multiphoton absorption upon strong and ultrafast infrared laser excitation. *Journal of Applied Physics*, 101(8):083108, 2007.

[131] A. Brodeur and S. L. Chin. Ultrafast white-light continuum generation and self-focusing in transparent condensed media. *Journal of the Optical Society of America B*, 16(4):637–650, 1999.

[132] Emre Yce, Georgios Ctistis, Julien Claudon, Emmanuel Dupuy, Klaus J. Boller, Jean-Michel Grard, and Willem L. Vos. Competition between electronic kerr and free-carrier effects in an ultimate-fast optically switched semiconductor microcavity. *Journal of the Optical Society of America B*, 29(9):2630–2642, 2012.